

DM models, we will in the following mostly restrict our discussion, for definiteness, to the case of one universal extra dimension (UED) [20] in which all SM fields can propagate. In this case, the first KK excitation of the photon is a viable DM candidate [21–24] that has been intensely discussed in the literature – both in terms of prospects for accelerator searches [25–28] and direct DM detection [29–32], as well as indirect DM searches with gamma rays [8, 14, 33, 34], positrons [35–37], neutrinos [38–41] or antiprotons [42, 43] (for a review, see Ref. [44]). The relevance of resonances for the DM phenomenology of this model [45] has been explored in detail for both collider searches [46–48] and precision computations of the relic density [48–51]. In this article, we demonstrate that resonances can be at least as important for indirect detection, and calculate annihilation rates for processes that produce pronounced spectral signatures in gamma rays.

We study various situations of interest where the full velocity-dependence of the annihilation rate must be taken into account. For DM annihilation in the Galactic halo, e.g., averaging over the DM velocity distribution can significantly enhance the annihilation rate into monochromatic photons, compared to the $v \rightarrow 0$ limit, even for small average velocities. A supermassive black holes (SMBH) like the one at the Galactic center (GC), on the other hand, can act as an effective DM particle accelerator with CMS energies many times above the rest mass [52, 53]. Whether the effect of those high-energy collisions close to the horizon is actually observable far away from the black hole (BH) [54–59], or rather not [60–62], is a matter of ongoing debate. Here, we point out that if the annihilation rate is sufficiently large, upcoming GC observations at TeV energies by HESS [63] or CTA [64] may indeed reveal the unique and striking spectral signature of a line ‘forest’ that we have already mentioned above.

This article is organised as follows. We start by introducing the UED model in Sec. II, with a particular focus on its minimal version. The resulting gamma ray spectrum from KK DM is then addressed in Sec. III, including in particular a detailed discussion of the hitherto neglected contributions from various resonances in the relevant annihilation cross sections. Next, we introduce in Sec. IV the astrophysical setup that is required to translate annihilation rates into the expected gamma ray flux, including a short discussion about DM halo density and velocity distributions. In Section V we apply this formalism to our results from Sec. III in order to assess the impact of a non-vanishing, but still not highly relativistic, DM velocity on the gamma ray signal from KK DM. Section VI then focuses on the more optimistic case of highly relativistic DM particles accelerated by SMBHs – which offers, as we will see, the possibility of a particularly striking signature in gamma rays. In Sec. VII, finally, we summarize our results and conclude. The technical details on the calculation of the annihilation process are given in Appendices A, B and C, while the details for

the photon flux from the region around a BH can be found in Appendix D.

II. UNIVERSAL EXTRA DIMENSIONS

The UED model is essentially a higher-dimensional version of the SM of particle physics, i.e. all SM fields are allowed to propagate in one or more compactified extra dimensions [20]. Since the SM in $d > 4$ is not renormalizable, this must be understood as an effective field theory which is only valid up to a cutoff scale Λ . We will restrict our discussion in the following to the simplest case of one UED, where the extra dimension is compactified on an S^1/\mathbb{Z}_2 orbifold. The orbifold construction is essential to both recover the chiral structure of the 4D effective theory, which is non-trivial in view of the fact that chiral fermions do not exist in 5D, and to prevent unwanted light degrees of freedom that correspond to the higher-dimensional components of gauge fields.

5D fields, or rather all their components with a well-defined behavior under 4D Lorentz transformations, can then be expanded as either

$$\Phi(x^\mu, y) = \frac{1}{\sqrt{2\pi R}} \phi^{(0)}(x^\mu) + \frac{1}{\sqrt{\pi R}} \sum_{n=1}^{\infty} \phi^{(n)}(x^\mu) \cos \frac{ny}{R} \quad (1)$$

or

$$\Phi(x^\mu, y) = \frac{1}{\sqrt{\pi R}} \sum_{n=1}^{\infty} \phi^{(n)}(x^\mu) \sin \frac{ny}{R}, \quad (2)$$

depending on whether one assigns even (1) or odd (2) transformation properties under the orbifold projection $y \rightarrow -y$. Here and in the following, x^μ denote ordinary 4D space-time co-ordinates, y the extra dimensional direction and R the compactification radius. Each 5D Φ thus corresponds to a whole tower of heavy states $\phi^{(n)}$ in the effective 4D theory that is obtained after integrating out the extra dimension; only even states, however, have a light zero mode $\phi^{(0)}$ (which is identified with the corresponding SM field).

In this way, each SM gauge field A_μ is accompanied by a tower of KK states, $A_\mu^{(n)}$, and each fermion ψ by *two* towers that represent $SU(2)$ doublets, $\psi_d^{(n)}$, and singlets, $\psi_s^{(n)}$, respectively. As for the scalar sector, there is the SM Higgs field h and its KK tower $h^{(n)}$; further physical states $a^{(n)}$ and $a_\pm^{(n)}$ arise at $n \geq 1$ as linear combinations of the higher-dimensional components of the $SU(2)_L \times U(1)_Y$ gauge fields and would-be Goldstone bosons of the Higgs doublet. Up to the first KK-level, $n \leq 1$, the spectrum of states is thus the same as in the minimal supersymmetric standard model, up to the spin properties of the SM partners, which is why the UED model has sometimes also loosely been referred to as ‘bosonic supersymmetry’ [65].

As a direct consequence of momentum conservation along the extra dimension, KK number is conserved at

tree level. Every tree-level vertex involving particles with KK number n_i must thus obey one of the selection rules implied by $\sum \pm n_i = 0$. At higher orders in perturbation theory, on the other hand, this is not necessarily the case because the orbifold fixpoints break the original 5D translational invariance. One of the phenomenologically most important consequences of the orbifold compactification, however, is that KK-parity, defined as $(-1)^{\sum_i n_i}$, is still conserved.¹ This remnant of the original 5D translational invariance implies that the lightest Kaluza-Klein particle (LKP) is stable and thus a potential DM candidate (in the very same fashion as the lightest supersymmetric particle is stable if R -parity is conserved). For our discussion, however, the actual mass spectrum is not only crucial for determining the LKP but also because it determines both the exact location of resonances and which decay processes are kinematically allowed.

At tree level, the mass of a KK-state is given by

$$M_{(n)}^i = m_{\text{EW}}^i + \left(\frac{n}{R}\right)^i, \quad (3)$$

where $i = 2$ ($i = 1$) for bosons (fermions) and m_{EW} is the mass of the corresponding SM state, generated by electroweak symmetry breaking. Current collider data constrain the compactification scale to $R^{-1} \gtrsim 700 \text{ GeV}$ [66–68], with stronger limits applying for $d > 5$. One thus generically expects very degenerate spectra at any given KK level, due to $R^{-1} \gg m_{\text{EW}}$, which implies that radiative mass corrections $\delta M_{(n)}$ become important to determine the actual mass hierarchy of states. Those corrections on top of the SM contributions (which are renormalized in the usual way) arise both due to winding modes of loops in the bulk and due to terms localized at the orbifold boundaries [21, 69, 70]. The latter are formally infinite and thus need to be renormalized by counter-terms with in general unknown finite parts.

The scenario of *minimal* UED (mUED) rests on the simplifying assumption that those terms at the orbifold boundaries can be neglected at the cutoff scale Λ ; all KK masses are then uniquely determined by only two parameters Λ and R [21]. For the recently determined Higgs mass of $m_h \sim 125 \text{ GeV}$ [71, 72], however, the running of the Higgs self-coupling implies an unstable vacuum unless the cutoff scale is as small as $\Lambda R \sim 5$ [51, 68, 73]. In the mUED scenario, the LKP is the first KK excitation of the photon, which to a very good approximation is the same as the first KK excitation of the hypercharge gauge boson, $B^{(1)}$. As it turns out, the $B^{(1)}$ is indeed an excellent DM candidate [23]. Thermal production in the early universe leads to the correct relic density for $R^{-1} \simeq m_{B^{(1)}} \sim 1.2 \text{ TeV}$ [51, 74], a compactification scale that may well be in reach for the LHC after its upgrade [22]. Taking into account the requirement of relic

density and vacuum stability, there are thus essentially no free parameters in the simplified UED scenario known as mUED.

The interaction terms localized at the orbifold fixpoints, however, are in principle arbitrary (though their scale-dependence is determined by bulk interactions). At a given scale, they should thus in general simply be viewed as new free parameters of the theory. In particular, those parameters should follow from some more fundamental theory at energies $E \gtrsim \Lambda$ and there is no obvious reason why such a theory should predict all those terms to vanish at the cutoff scale. Compared to the mUED scenario, non-vanishing boundary terms will affect the corrections to the self-energies, and thus the mass hierarchy, of KK particles. In fact, in non-minimal UED scenarios, one may explicitly allow even for bulk mass terms [75]. An often adopted approach is therefore to treat the mass splittings $\delta M^{(n)}$ as essentially free parameters. We note that this could even change the nature of the LKP [76], but leave an investigation of possible consequences of this interesting possibility for future work. Changing the mass-splittings of the KK particles can have significant effects on the compactification scale that results in the correct relic density for a $B^{(1)}$ LKP. The lowest possible value is given by $R^{-1} \sim 800 \text{ GeV}$ and corresponds to mass splittings much larger than in the mUED case, such that co-annihilations are no longer important [23]. Tuning the mass spectra to be highly degenerate, on the other hand, makes co-annihilations even more important and may drive the compactification scale, and thus mass, of a thermally produced $B^{(1)}$ LKP up to a value of a few TeV [77, 78]. Finally, let us stress that the cutoff scale will in general be significantly larger than the value of $\Lambda R \sim 5$ implied by vacuum stability in the simplified mUED scenario.

III. PHOTONS FROM KK DARK MATTER

A. Spectrum in the zero-velocity limit

The expected gamma ray spectrum from the annihilation of $B^{(1)}$ pairs to SM model particles has been extensively studied in the literature. First of all, there is the usual *secondary* contribution to the spectrum from $B^{(1)} B^{(1)} \rightarrow \bar{q}q, ZZ, W^+W^-$ [33] that results from the fragmentation and decay of the annihilation products, mostly via $\pi^0 \rightarrow \gamma\gamma$. Unlike the typical situation in supersymmetry, also the decay of τ leptons gives an important contribution and leads to a significantly harder spectrum [8] as a result of the relatively large $B^{(1)} B^{(1)} \rightarrow \tau^+ \tau^-$ rate.

In fact, the annihilation into lepton final states is the dominant channel, with roughly the same branching fraction of $\sim 20\%$ for all lepton families. An even more important contribution at the phenomenologically most relevant highest energies, i.e. close to the kinematic endpoint of $E_\gamma = m_\chi$, are thus *primary* photons

¹ This can be traced back to the invariance of (1,2) under reflection about the center ($y = \pi R/2$) of the extra-dimensional interval.

radiated off lepton final legs [8]. This final state radiation (FSR) is dominated by collinearly emitted photons, resulting in a universal spectrum of the Weizsäcker-Williams form [7, 8, 79]:

$$\frac{dN_\gamma^{\text{FSR}}}{dx} \equiv \frac{1}{\sigma_{B^{(1)}B^{(1)} \rightarrow \ell^+\ell^-}} \frac{d\sigma_{B^{(1)}B^{(1)} \rightarrow \ell^+\ell^-\gamma}}{dx} \quad (4)$$

$$\simeq \frac{\alpha}{\pi} \frac{1 + (1-x)^2}{x} \log\left(\frac{s(1-x)}{m_\ell^2}\right). \quad (5)$$

Here, $\sqrt{s} = 2m_{B^{(1)}}$ is the CMS energy and $x \equiv 2E_\gamma/\sqrt{s} = E_\gamma/m_{B^{(1)}}$. Overall, one expects a characteristic, relatively hard spectrum which drops abruptly at the DM mass; such a photon distribution could very efficiently be discriminated from typical astrophysical backgrounds [5].

An even more striking spectral feature would be the quasi-monochromatic line expected for $B^{(1)}B^{(1)} \rightarrow \gamma X$, at a photon energy of

$$E_\gamma = m_{B^{(1)}} \left(1 - \frac{m_X^2}{4m_{B^{(1)}}^2}\right). \quad (6)$$

Due to the large LKP mass, the three possible line signals (for $X = \gamma, Z, h$) would essentially be indistinguishable and thus simply add up in the spectrum (at $E_\gamma \simeq m_\chi$). A fully analytic one-loop calculation has been performed for the dominant process of $B^{(1)}B^{(1)} \rightarrow \gamma\gamma$ via fermion box diagrams [14]. Numerical calculations have both confirmed and extended these analytic results [34], as well as estimates [14] for the subdominant annihilation channels into γZ and γh final states. In order to discriminate the monochromatic signal from the continuum FSR photon signal discussed above, given an expected total annihilation cross section of $(\sigma v)_{\gamma X} \lesssim 10^{-29} \text{ cm}^3/\text{s}$, requires the energy resolution of the detector to be better than a few percent [14]. While such a performance is, unfortunately, unfeasible for both operating and upcoming Air Cherenkov Telescopes, which feature energy resolutions of 10-15%, it might be well in reach for space-based telescopes given the design characteristics of planned missions like Gamma-400 [80], DAMPE [81] or CALET [82].

It is worth stressing that the continuous gamma ray spectrum from annihilating $B^{(1)}$ pairs is rather insensitive to the other KK masses, such that one expects essentially the same spectrum even in non-minimal UED scenarios. The strength of the line signal, on the other hand, can be enhanced by a factor of a few when allowing for smaller mass differences between KK fermions and the $B^{(1)}$ [14] (and can be much larger for other LKP candidates, such as the $Z^{(1)}$ [83]).

B. Annihilation rate revisited

Let us now address the question of how the above presented situation changes when allowing for a non-zero relative velocity of the annihilating LKP pair. The

first thing to note is that the FSR continuum spectrum dN^{FSR}/dx will not change visibly if, as already indicated in Eq. (5), one uses the actual CMS energy rather than $2m_{B^{(1)}}$ in defining the dimension-less photon energy x . The same is true for the secondary photons, given that s is the only scale in the problem (provided that, as is the case of interest here, the CMS energy is much larger than the mass of any of the annihilation products). Unless one is in the highly relativistic regime, furthermore, one can expect even the normalization of the spectrum to stay roughly constant because the $B^{(1)}$ is an s -wave annihilator with a total annihilation cross section of

$$\sigma v_{\text{rel}} \simeq 3 \times 10^{-26} \text{ cm}^3 \text{ s}^{-1} \left(\frac{m_{B^{(1)}}}{800 \text{ GeV}}\right)^{-2}, \quad (7)$$

where both σv and the final state branching ratios are rather insensitive to the spectrum of other KK states [42]. The same expectations hold for the line signals discussed above: while the location of the line will shift from $E_\gamma \simeq m_\chi$ to $E_\gamma \simeq \sqrt{s}/2$, its normalization will stay roughly the same as long as the CMS energy is not significantly larger than the rest mass of the two annihilating LKPs.

There is one important exception to these considerations and this is what we will focus on in the following: the appearance of s -channel *resonances* may significantly enhance the annihilation rate with respect to the zero velocity limit (in which case s -channel diagrams give subdominant contributions for both the line and continuum signals). A further advantage of these resonances is that they add a scale to the process, which in general is the only way to preserve a sharp spectral feature in the potentially observable gamma ray flux after integrating over a *distribution* of CMS energies or relative velocities (see also Section IV).²

For at least three reasons, these observations are particularly relevant for the case of KK DM:

1. Due to the mass degeneracy of KK states, relevant resonances are naturally expected for level-2 KK states in the s -channel.
2. The decay of these resonances into SM states is necessarily loop-suppressed because it violates KK number conservation. This implies very narrow widths, and thus large enhancements on resonance, if the decay to level-1 KK states is kinematically forbidden or otherwise suppressed (which, as discussed below, often is the case).

² This is most easily seen for the case of a monochromatic line: integrating $d\sigma/dE_\gamma \equiv N \delta(E_\gamma - \sqrt{s}/2)$ over some – astrophysically motivated and typically featureless – CMS energy distribution $f(s)$ simply results in a flux proportional to $f(2E_\gamma)$ for an energy-independent normalization N ; the initial line-feature is thus completely smeared out. If, on the other hand, N is strongly peaked, at the energy of the resonance, a pronounced peak at the same energy will also show up in the flux – independently of the functional form of f .

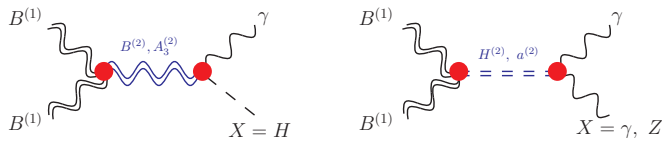


FIG. 1. Diagrams that generally lead to the most pronounced spectral features in the UED scenario when allowing for relative WIMP velocities $v \neq 0$. The blobs correspond to effective couplings that are computed in Appendices A and B.

- Another consequence of a loop-suppressed total width is that continuum and monochromatic photons are produced at roughly the same strength on resonance, unlike the typical situation where only the line signal is loop-suppressed. In other words, one can expect a much larger *relative* enhancement of the line signals (which, as discussed above, is not the least needed to overcome the large contribution from FSR photons).

In the UED scenario, resonances thus indeed single out spectral features in a unique way.

With these general considerations in mind, let us now turn to a more detailed discussion of which resonances will be most relevant in our case. Charge conservation implies that for the annihilation of a $B^{(1)}$ pair the only possible resonances at KK-level 2 are the vector bosons $B^{(2)}$, $A_3^{(2)}$ and the scalars $H^{(2)}$, $a_0^{(2)}$. In Fig. 1, we show the corresponding Feynman diagrams. Here, the blobs on the left represent effective $B^{(1)}B^{(1)}Y^{(2)}$ couplings that may either exist at tree level or correspond to 1-loop subdiagrams. The right blob represents a KK-number violating coupling and is thus necessarily loop-suppressed. However, not all combinations of resonance states $Y^{(2)}$ and final states γX are actually possible. For a scalar resonance, for instance, X must be a vector in order to conserve helicity. Vector resonances, on the other hand, are only allowed for $X = H$: the $\gamma\gamma$ annihilation channel is forbidden by the Landau-Yang theorem [84, 85]; γZ final states cannot appear due to the anomaly cancellation familiar from the SM, which prevents anomalous three-gauge-boson couplings. For a very similar reason, in fact, it turns out that the $a_0^{(2)}$ resonance cannot decay into two vectors either (recall that a_0 contains the fifth component of the higher-dimensional Z boson).

The obvious next step consists in identifying which of the remaining processes are most relevant in producing line signals. To do so, it is instructive to have a closer look at the actual mass spectrum of the involved states. In Fig. 2, we show in the left column the mass of the relevant resonant particles $Y^{(2)}$ (in units of *twice* the inverse compactification scale R^{-1}). For comparison, the middle and right column show the mass of first-level excitations. The first thing to note is that the tree-level decay of $Y^{(2)}$ into KK-1 states is in some cases not kinematically possible, or at least heavily suppressed. The decay width

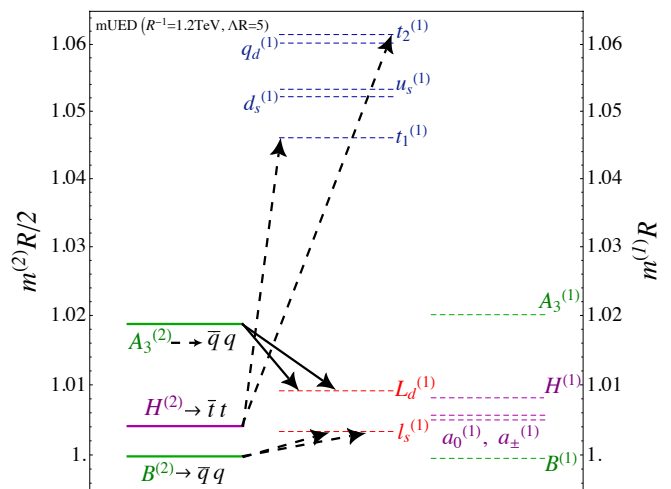


FIG. 2. Mass spectrum of relevant KK(2) resonances in the mUED scenario, in units of *twice* the inverse compactification scale R^{-1} (left column). The middle and right columns show the mass of KK(1) states; note that only for the KK top quark the mass eigenstates $(t_1^{(1)}, t_2^{(1)})$ differ significantly from the flavor eigenstates $(t_s^{(1)}, t_d^{(1)})$. Dominant decay channels in the mUED case are displayed by solid arrows unless the resonance mainly decays to SM particles. Dashed arrows indicate the dominant decay process in non-minimal UED versions.

Resonance $Y^{(2)}$	$B^{(2)}$	$A_3^{(2)}$	$H^{(2)}$
$Y^{(2)} \rightarrow \gamma X$	γH ($\Gamma \sim 0.07$)	γH ($\Gamma \sim 0.07$)	$\gamma\gamma, \gamma Z$ ($\Gamma \sim 0.12, 0.36$)
$\Gamma_{Y^{(2)}}^{\text{main}}$ (mUED)	$\bar{f}_{\text{SM}} f_{\text{SM}}$ ($\Gamma \sim 0.8$)	$\bar{l}_d^{(1)} l_d^{(1)}$ ($\Gamma \sim 70$)	$\bar{t}t$ ($\Gamma \sim 0.1$)
$\Gamma_{Y^{(2)}}^{\text{main}}$ (non-mUED)	$\bar{f}_{d,s}^{(1)} f_{d,s}^{(1)}$ ($\Gamma \sim 15$)	$\bar{f}_{\text{SM}} f_{\text{SM}}$ ($\Gamma \sim 0.8$)	$\bar{t}_{d,s}^{(1)} t_{s,d}^{(1)}$ ($\Gamma \sim 160$)
$B^{(1)}B^{(1)}Y^{(2)}$	$\sim g'^3 m_t$	$\sim g'^2 g m_t$	$\sim g'^2 g^{-1} m_W$

TABLE I. Main decay channels, couplings and possible γX final states for the resonances shown in Fig. 1 (note that $\Gamma_{a_0^{(2)} \rightarrow \gamma\gamma, \gamma Z} = 0$). Decay rates are given in GeV and obtained for $R^{-1} = 1.2$ TeV and $\Lambda R = 5$; see Appendix A for calculational details.

for those particles is therefore instead determined by the loop-suppressed decay into two SM particles; such a narrow width will correspondingly enhance the LKP annihilation rate on resonance. The dominant decay channels are shown in the figure and also summarized in Tab. I. For comparison, we also indicate how this would change if all final states were kinematically accessible, as can be arranged in non-minimal UED scenarios (for the case of the $A_3^{(2)}$ resonance, we show instead the dominant decay to SM particles if the decay into KK(1) leptons was *not*

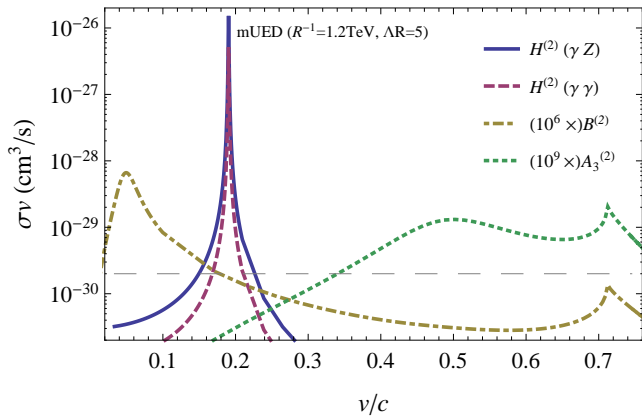


FIG. 3. $B^{(1)}B^{(1)} \rightarrow \gamma X$ cross sections in the mUED scenario, for the various channels considered in Fig. 1, as a function of the relative speed of the WIMPs (the curves associated with the $B^{(2)}$ and $A_3^{(2)}$ resonances are multiplied by factors 10^6 and 10^9 respectively). The horizontal dashed line indicates the dominant line signal in the zero-velocity limit, which arises from $B^{(1)}B^{(1)} \rightarrow \gamma\gamma$ [14]. Note that the *location* of the resonances is essentially a free parameter in UED theories; in particular, it can occur at much smaller velocities than shown here for the mUED case.

kinematically allowed). The other important parameters to take into account are clearly the (effective) couplings that appear in Fig. 1. In Tab. I, we thus also indicate for reference the size of the (effective) $B^{(1)}B^{(1)}Y^{(2)}$ coupling as well as the decay rate $Y^{(2)} \rightarrow \gamma X$. From this overview, it becomes clear that the $H^{(2)}$ resonance is clearly expected to result in the strongest line signal: it is not only the most long-lived resonance, but also the only one that couples to the incoming LKP pair at tree level.

We have performed a full calculation of the dominant contribution to all annihilation processes shown in Fig. 1, which includes a determination of the relevant effective couplings and decay rates (for details, see Appendices A and B). In Fig. 3, we show the individual contributions to the cross section for $B^{(1)}B^{(1)} \rightarrow \gamma X$ from these diagrams. Note that the ratios of the peak values agree well, within an order of magnitude, with the naive estimates one can infer directly from the values stated in Tab. I. In particular, the by far largest cross section for a monochromatic photon can be obtained for $B^{(1)}B^{(1)} \xrightarrow{H^{(2)}} \gamma Z$, with a very pronounced resonance corresponding to the mass of the $H^{(2)}$. Remarkably, this cross section (as well as the corresponding process for $\gamma\gamma$ final states) can be significantly larger than the cross section for $B^{(1)}B^{(1)} \rightarrow \gamma X$ in the zero velocity limit as indicated by the dashed line, $\sigma v = 2 \times 10^{-30} \text{ cm}^3/\text{s}$. In fact, even at $v = 0$, the $H^{(2)}$ resonance thus contributes at roughly the same level as γZ final states without taking into account these contributions [14, 34]. While the *locations* of the resonances are specific to the mUED scenario, the couplings are typically only affected at the level of radiative corrections for de-

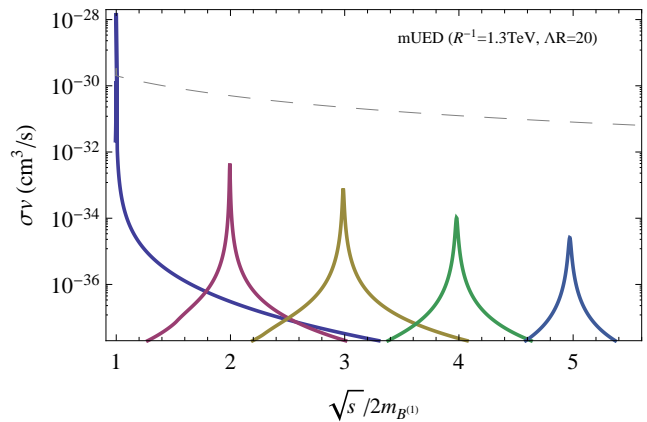


FIG. 4. Contributions of the first five $H^{(2n)}$ resonances to the $B^{(1)}B^{(1)} \rightarrow \gamma Z$ annihilation rate in the mUED scenario, taking however $\Lambda R = 20$, as a function of $\sqrt{s}/2m_{B^{(1)}}$. The dashed line is an extrapolation ($\propto s^{-1}$) of the standard result for $B^{(1)}B^{(1)} \rightarrow \gamma\gamma$ [14]. Note that in general one can encounter much larger peak normalizations than what is shown here for the *minimal* UED case.

viations from the minimal scenario; this implies that the *signal strengths* shown in this figure are rather generic. A possible exception to this last comment would occur if the mass spectrum displayed in Fig. 2 would change in a qualitative way, opening up new or closing existing decay channels. An interesting possibility to even further enhance the $B^{(1)}B^{(1)} \rightarrow \gamma X$ rate beyond the mUED expectation would also be to increase the mixing between the KK top quark states beyond its mUED value of $\sin 2\alpha_t^{(1)} = 0.143$, a quantity which enters quadratically in the cross section (B3, B4).

So far, we have only mentioned the effect of second-level KK resonances. As discussed in Section VI later on, however, there may exist extreme astrophysical environments where much higher CMS energies are available for the collision of two LKPs. If those energies are sufficient to excite higher KK resonances $Y^{(2n)}$, with $n > 1$, this would lead to a rich phenomenology. While we do not aim at an exhaustive discussion here, we would like to point out that most of the arguments presented above can straightforwardly be applied to this situation as well. One of the most striking consequences, however, may in any case be the appearance of *multiple gamma ray lines with an equidistant spacing in energy* that equals almost exactly twice the inverse of the compactification radius, $\Delta E_\gamma^{\text{line}} \simeq 2/R$: if such a striking spectral signature would be observed, this would constitute a smoking gun signal for the higher-dimensional origin of the cosmological DM.

In Fig. 4, we show explicitly that such a structure indeed appears in the mUED model.³ While $H^{(2n)}$ reso-

³ Note that in order to demonstrate this effect, we have allowed

nances dominate over other resonances also at $n > 1$, however, their contribution to the annihilation cross-section is a few orders of magnitude smaller than that of the first resonance (shown in more detail in Fig. 3). This is mainly due to two reasons. First, in contrast to the tree-level coupling between $H^{(2)}$ and the two incoming LKPs, the corresponding couplings of higher-level $H^{(2n)}$ are radiatively generated and localized at the orbifold fixed points – see Appendix C 2 for an exhaustive discussion on radiative vertices in UED. Secondly, higher-level KK states have more possible decay modes and it is thus less likely that there is no kinematically allowed channel at tree-level. As discussed above, the resulting larger decay widths thus decrease the expected peak annihilation rate. Relaxing the restrictive assumptions of the mUED model, however, both these caveats can be overcome: allowing large boundary terms at the cut-off scale that prevent the $B^{(1)}B^{(1)}H^{(2n)}$ ($n > 1$) vertex from being strictly radiative, while keeping the vertices relevant for the $H^{(2n)}$ decay small, would boost these resonances to a level which can be fairly comparable to the one encountered in the $H^{(2)}$ case.

To summarize this Section, we have pointed out the remarkable fact that resonances in extra-dimensional DM models may naturally enhance monochromatic gamma ray lines much more than the continuum signal of secondary and FSR photons. In the mUED model, this leads to a line signal which for DM velocities $v \sim \mathcal{O}(0.1)$ can be enhanced by several orders of magnitude with respect to the $v = 0$ limit known from the literature. As we have stressed, however, there is no particularly strong reason to adopt the restrictive limitations of the minimal model. In fact, UED scenarios generally allow for resonances at considerably smaller relative velocities of the annihilating DM particles and, to a lesser degree, there is also some freedom to enhance the signal normalization even further. Potentially even more important, these scenarios allow for the appearance of multiple strong line signals at equally spaced photon energies.

IV. GAMMA RAY FLUX FROM DM ANNIHILATION

Neglecting for the moment relativistic effects, the expected gamma ray flux from DM annihilation from a direction ψ , averaged over the opening angle $\Delta\psi$ of the

detector, is given by:

$$\frac{d\Phi}{dE_\gamma}(E_\gamma, \psi) = \frac{1}{8\pi} \int_\psi \frac{d\Omega}{\Delta\psi} \int_{\text{l.o.s}} dl(\psi) \rho^2(\mathbf{r}) \times \frac{1}{m_{\text{DM}}^2} \left\langle \sigma v_{\text{rel}} \sum_f B_f \frac{dN_\gamma^f}{dE_\gamma} \right\rangle, \quad (8)$$

where the integration is performed along the line of sight (l.o.s) and we take into account that the DM particles are self-conjugate (for DM candidates with distinct particle and anti-particle there would be an additional factor of 1/2). The spatial distribution of the signal traces the DM density profile $\rho(r)$ and is typically assumed to be fully determined by the quantity $J(\psi) \equiv \int_\psi d\Omega/\Delta\psi \int_{\text{l.o.s}} dl(\psi) \rho^2(r)$. The second line of Eq. (8) contains the particle physics of the underlying theoretical model, as discussed in the previous Section: the velocity-weighted CMS annihilation cross section σv_{rel} at present time, the branching ratio B_f into channel f , times the number of photons N_γ^f produced per annihilation; this factor determines the spectral shape of the signal.

The velocity-average that appears above is given by

$$\langle f(v_{\text{rel}}) \rangle \equiv \int d^3v_1 d^3v_2 P_{\mathbf{r}}(\mathbf{v}_1) P_{\mathbf{r}}(\mathbf{v}_2) f(v_{\text{rel}}) = \int d^3v_{\text{rel}} P_{\mathbf{r},\text{rel}}(\mathbf{v}_{\text{rel}}) f(v_{\text{rel}}) \quad (9)$$

$$\equiv \int dv_{\text{rel}} p_{\mathbf{r},\text{rel}}(v_{\text{rel}}) f(v_{\text{rel}}), \quad (10)$$

where $P_{\mathbf{r}}(\mathbf{v}_i)$ is the 3D normalized velocity distribution function of a WIMP at a position \mathbf{r} and

$$P_{\mathbf{r},\text{rel}}(\mathbf{v}_{\text{rel}}) \equiv \int d^3v_{\text{CM}} P_{\mathbf{r}}(\mathbf{v}_{\text{CM}} + \mathbf{v}_{\text{rel}}/2) P_{\mathbf{r}}(\mathbf{v}_{\text{CM}} - \mathbf{v}_{\text{rel}}/2) \quad (11)$$

is the 3D distribution function of the relative velocities of the WIMPs, with $\mathbf{v}_{\text{rel}} \equiv \mathbf{v}_1 - \mathbf{v}_2$ and $\mathbf{v}_{\text{CM}} \equiv (\mathbf{v}_1 + \mathbf{v}_2)/2$. For a Maxwell-Boltzmann (MB) distribution $p_{\mathbf{r}}(\mathbf{v}) = 4\pi^{-\frac{1}{2}} v_0^{-3} v^2 \exp[-v^2/v_0^2]$ with most probable velocity v_0 , for example, $p_{\mathbf{r},\text{rel}}(\mathbf{v}_{\text{rel}})$ is given by an MB distribution with most probable velocity $\sqrt{2}v_0$.

Let us stress that in general the particle physics factor in Eq. (8) cannot be factorized out of the integral along the line of sight, because an implicit \mathbf{r} -dependence enters via the velocity-average over $P_{\mathbf{r},\text{rel}}(\mathbf{v}_{\text{rel}})$. In our case, the gamma ray flux thus depends on both the density and velocity distribution profile of the DM particles – in contrast to the typically assumed situation of a velocity-independent cross section.

The general expression (8) simplifies for the monochromatic photons emitted by the annihilation of LKP pairs we consider here. The differential cross section near a strong resonance, in particular, is given by

$$\sigma \sum_f B_f \frac{dN_\gamma^f}{dE_\gamma} \simeq \frac{N_\gamma \sigma_{\text{res}} \Gamma_{\text{res}}^2 m_{\text{res}}^2}{(s - m_{\text{res}}^2)^2 + \Gamma_{\text{res}}^2 m_{\text{res}}^2} \delta\left(E_\gamma - \frac{\sqrt{s}}{2}\right), \quad (12)$$

for a larger cutoff value $\Lambda R = 20$, which can be motivated by slightly non-minimal boundary terms affecting the Higgs self-coupling and thus circumventing the arguments from vacuum stability that lead to $\Lambda R \sim 5$.

where m_{res} and Γ_{res} are the mass and width of the s -channel particle, respectively, σ_{res} is the peak value of the cross section and we have neglected the masses of the final state particles; $N_\gamma = 2$ for $\gamma\gamma$ final states and $N_\gamma = 1$ otherwise. Given that $s = 4m_{\text{DM}}^2/(1 - v_{\text{rel}}^2/4)$ in the CMS system, the velocity-average can be evaluated trivially and the flux near the resonance becomes

$$\frac{d\Phi_{\text{res}}}{dE_\gamma} \simeq \frac{N_\gamma (\sigma v_{\text{rel}})_{\text{res}}}{8\pi E_\gamma^3} \frac{\tilde{J}_{\text{line}}(E_\gamma) \Gamma_{\text{res}}^2 m_{\text{res}}^2}{(4E_\gamma^2 - m_{\text{res}}^2)^2 + \Gamma_{\text{res}}^2 m_{\text{res}}^2}, \quad (13)$$

where

$$\tilde{J}_{\text{line}}(E_\gamma) \equiv \frac{1}{\Delta\Omega} \int_{\Delta\Omega} d\Omega \int_{\text{l.o.s.}} dl \int \rho^2(\mathbf{r}) \frac{p_{\mathbf{r},\text{rel}}(v_{\text{rel}}^{\text{line}})}{v_{\text{rel}}^{\text{line}}/4} \quad (14)$$

and $v_{\text{rel}}^{\text{line}}(E_\gamma) = 2\sqrt{1 - m_{\text{DM}}^2/E_\gamma^2} \simeq \sqrt{8}\sqrt{E_\gamma/m_{\text{DM}} - 1}$.

Before discussing in more detail the implications for the UED model, however, let us in the following subsections briefly describe the DM density profile and the DM velocity distribution in a halo that enter in the above expressions.

A. DM density profile

A generic parametrization for a spherically symmetric DM density, that encompasses several halo profiles, is given by:

$$\rho(r) = \rho_\odot \left(\frac{r}{r_\odot} \right)^{-\gamma} \left[\frac{1 + (r_\odot/r_0)^\alpha}{1 + (r/r_0)^\alpha} \right]^{\frac{\beta-\gamma}{\alpha}}, \quad (15)$$

where $\rho_\odot \simeq (0.3 - 0.4) \text{ GeV/cm}^3$ [86, 87] is the DM density in the solar neighborhoods and $r_\odot \simeq 8.5 \text{ kpc}$ denotes the Sun's position with respect to the GC. In our analysis we consider the two density profiles with the extreme opposite behavior in the inner part. The NFW density profile [88] is obtained for $(\alpha, \beta, \gamma) = (1, 3, 1)$ and a scale radius of $r_0 = 20 \text{ kpc}$. Such a cuspy profile is favored by numerical N -body simulations; for very small galactocentric distances, $r \lesssim 100 \text{ pc}$, the profile may in fact be even steeper and exhibit a slope of $\rho \propto r^{-1.2}$ [89–91]. On the contrary the cored isothermal profile – which is observationally inferred for low surface brightness as well as dwarf galaxies [92, 93] – has $(\alpha, \beta, \gamma) = (1, 2, 1)$, a scale radius of 3.5 kpc and a finite density core close to the GC.

It is very likely that the central SMBHs in galaxies have primordial DM density spikes [94]. When indeed a BH forms, the DM distribution adjusts to the new gravitational potential and this process leads to the formation of spikes. Even though gravitational scattering off stars of DM particles and DM annihilation [95, 96] tend to reduce the DM density in spikes, the enhancement is still significant with respect to ordinary cuspy profiles. This leads to a change in the slope $\gamma \rightarrow \gamma' = 7/3$ of the density

profile within the BH radius of influence for a NFW profile (prior to BH formation), with a plateau at a radius where annihilations become important over the BH lifetime. GR corrections to the profile for the Schwarzschild case are computed in [97], where the inner radius of the annihilation plateau is found to be $2r_S$, where r_S is the Schwarzschild radius of the BH. The extent to which the spikes survive dynamical heating by their environment is unknown. We consider the pessimistic case described in [98], where an initially $\gamma' = 3/2$ profile is adopted, arising from a cored isothermal profile. In other words, in the case of the GC, stellar scattering affects the BH spike over several core relaxation times, amounting to a few Gyr. Hence the density profile is most likely softened to a $\gamma' \sim 3/2$ profile [99]. However more massive SMBH dynamical relaxation via stellar interactions does not occur, because the core relaxation time-scales are much longer. In the case of M87, which we will discuss later as one of our most promising candidates, the core-related time-scale is of order 10^5 Gyr . Hence the initial spike profile is preserved.

More quantitatively, consider a DM density spike surrounding a massive BH. There are several scales of interest. The gravitational radius of influence, which by definition contains the same mass as the BH, and the half-mass radius of the spheroid are respectively:

$$\begin{aligned} r_i &= \frac{GM_{\text{BH}}}{\sigma^2}, \\ r_{1/2} &= \frac{GM_{1/2}}{\sigma^2}, \end{aligned} \quad (16)$$

where σ is the bulge velocity dispersion. The density profile is then given by

$$\rho \propto \begin{cases} r^{-\gamma} & \text{if } r > r_i, \\ r^{-\gamma'} & \text{if } r < r_i. \end{cases} \quad (17)$$

Efficient annihilation sets an upper limit on the DM density in the innermost parts. A density plateau, with $\rho_p \equiv \rho(r \lesssim r_p)$, thus occurs at a radius r_p where the annihilation timescale equals the BH age, $t_{\text{BH}} \sim 10^8 - 10^{10}$ years, i.e. where

$$\rho(r_p) (\sigma v_{\text{rel}}) = \frac{m_{\text{DM}}}{t_{\text{BH}}}. \quad (18)$$

B. Velocity distribution

By definition the density profile and the velocity distribution are related via

$$\rho(\mathbf{r}) = m_{\text{DM}} \int d^3v F(\mathbf{v}, \mathbf{r}), \quad (19)$$

where $F(\mathbf{v}, \mathbf{r})$ is the WIMP phase space distribution in the Galactic frame. Given a DM density profile, the underlying DM velocity distribution can be extracted by inverting Eq. (19) under the assumption of hydrostatic equilibrium, a solution known as the Eddington

formula [100]. The above integral can be inverted only under certain assumptions, such as spherical symmetry for the density profiles. For instance the MB distribution results from an isothermal density profile scaling as r^{-2} .

Other spherically symmetry density profiles, such as NFW, can be used to infer the corresponding velocity distribution and an application of this procedure for DM indirect detection is given in [101]. However it has been shown in [102] that the presence of baryons in N-body simulations has the effect of making the matter distribution more concentrated by adiabatic contraction, and the WIMP velocity distribution is brought closer to a MB distribution. Significant departure from the MB on the other hand arises when the velocity dispersion becomes small, e.g. close to the GC or in dwarf galaxies. In these regions, however, the main uncertainty derives from the inner slope of the density profile, which is difficult to extract from data and has not converged in simulations either. In fact, these N -body simulations indicate that DM halos are anisotropic and exhibit clumpy structures and streams, features that cannot be captured by the Eddington formula in a simple way. Going even closer to the central BH, where the DM spikes form, the assumption of hydrostatic equilibrium is not satisfied anymore: in this case, one would have to extract the DM velocity distribution from N -body simulations after adiabatic contraction. In order to avoid addressing in detail the large uncertainties involved in any brute force computation of the velocity distribution near the SMBH, we will in the following make the simplifying assumption of a MB distribution when considering DM particle collisions.

The old star population (> 1 Gyr) in the central 0.5 pc of our galaxy has a stellar cusp with relatively shallow slope $n(r) \propto r^{-\gamma}$, where $\gamma = 0.4 \pm 0.2$ [103], measured in a three-dimensional kinematic study. This slope is much flatter than the dynamically relaxed expectation ($\gamma = 3/2 - 7/4$) that we have adopted for the DM. The flattening is attributed to stellar heating. We note however that the recently discovered [104] young nuclear star cluster centered on SgrA* ($\gtrsim 50\%$ of the stars formed in the most recent star formation event 2 – 6 Myr ago) has a significantly steeper slope within its half-light radius of ~ 4 pc, comparable to the gravitational sphere of influence radius at ~ 3 pc. Because the BH has certainly grown by accretion of gas and stars over the past Gyr, it is not clear how the competing effects of adiabatic contraction of the DM, that steepens the profile, compete with dynamical heating. As discussed previously, the effects of stellar heating are irrelevant for SMBHs much more massive than in our galactic center, as is the case for M87 and Cen A. The three-dimensional kinematic study shows that the velocity field is consistent with that earlier inferred from orbital studies within 0.05 pc of SgrA* and yields a similar mass estimate for the central SMBH. Our simplifying assumption of a MB distribution should not modify our estimates of collision velocities by a significant factor compared to the other uncertainties in our model.

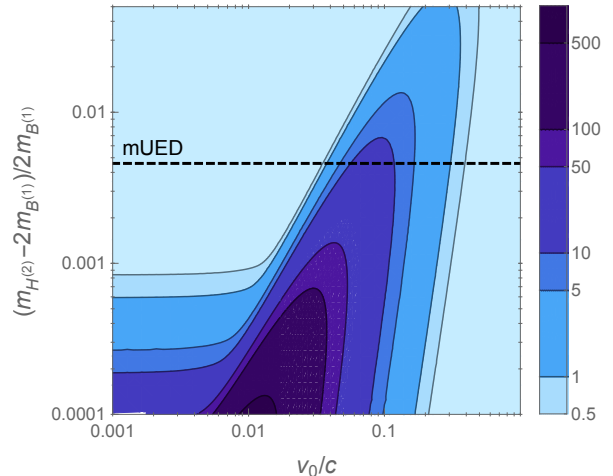


FIG. 5. Enhancement of the line signal due to the presence of resonances: the color scale indicates the ratio of the monochromatic photon flux resulting from the diagrams shown in Fig. 1, assuming a Maxwell-Boltzmann distribution with most probable DM velocity v_0 , to the one expected in the $v = 0$ limit. The dashed line indicates the mass difference between the resonance $H^{(2)}$ and twice the LKP $B^{(1)}$ in the minimal scenario (for $R^{-1} = 1.2$ TeV and $\Lambda R = 5$).

V. ENHANCED GAMMA RAY LINES FROM KK DM ANNIHILATION

Let us now assess in more detail by how much the line signal at $E_\gamma \sim m_{B^{(1)}}$ can be enhanced with respect to the $v = 0$ result in concrete applications. To this end, we assume a MB distribution for the WIMP velocities and compare the flux from resonant diagrams, as given by Eq. (13), with the flux in the zero velocity limit. The result is shown in Fig. 5 as a function of the resonance mass and the assumed velocity dispersion (using for example the velocity dispersion extracted from Fig. 18 of [101] instead of MB, based on an NFW profile with a baryonic bulge, does not qualitatively change our results). For an $H^{(2)}$ mass as given in the mUED scenario, indicated by the dashed line, the hitherto neglected diagrams will thus enhance the line signal by more than an order of magnitude for a most probable DM velocity of $v_0 \gtrsim 0.05$. Allowing for a smaller $H^{(2)}$ mass in non-minimal scenarios, on the other hand, will result in similar enhancements already for much smaller velocities. In the most favourable case, the signal may be up to three orders of magnitude stronger than expected from the calculation in the $v = 0$ limit.

It should be noted that the typical velocities in the *Milky Way* are of the order of $v \sim 10^{-3}$, such that there is seemingly little hope to actually observe resonant LKP annihilation on galactic scales (see, however, the next Section). Furthermore, current limits on monochromatic photons at TeV energies [105], deriving from observations

of the Galactic center, are almost three orders of magnitude weaker than the mUED signal expected in the $v = 0$ limit (though CTA will improve these limits by significantly more than one order of magnitude [106]). While s -channel annihilation will in general start to be important for mass differences between the $H^{(2)}$ mass and two times the LKP mass at the per mille level, as illustrated in Fig. 5, even more degenerate spectra would thus be needed to make the signal observable with near future technology.

The situation is considerably better for *galaxy clusters*, where the typical velocities of up to $v \sim 10^{-2}$ would be sufficient to probe the resonant regime for less non-minimal setups. Another advantage of clusters is that they are the astronomical targets for indirect DM searches with the largest mass hierarchy of (sub)sub halos, which implies that they maximise the signal enhancement due to substructures [107]. In optimistic scenarios for the distribution of substructures, they may thus be the brightest sources of DM annihilation radiation [108]. In combination with the enhancement from resonances studied here, line signals from clusters may thus offer a promising opportunity for DM detection with future Air Cherenkov telescopes like CTA.

Still, even the velocity dispersion of $0.008c$ measured in the most massive galaxy cluster known [109] appears relatively small in our context, and to really probe the extra-dimensional resonances even higher particle velocities are in general indispensable. Hence we turn next to an environment where there are known sources of high energy gamma rays and high particle collision velocities are inevitable, in the vicinity of SMBHs.

VI. GAMMA RAYS FROM DARK MATTER SPIKES: SCHWARZSCHILD BLACK HOLE CASE

SMBHs are found to be effective DM particle accelerators. Particle collisions occur to high CMS energies and are especially important for the case of a Kerr BH [53]. The CMS energy for particle collisions is limited to 4.5 times the rest mass for a Schwarzschild BH, in the case of Kerr attains energies of 20 times the rest mass for Kerr parameter⁴ $a = 0.998$, and is formally infinite for the extremal Kerr BH.

The following issues have been raised with regard to whether there is any potentially observable flux, namely whether the density spike survives, whether there is a negligibly small flux at infinity, whether back-reaction limits the acceleration, and whether the large red-shifting of photons generated in DM particle collisions renders any debris unobservable [60–62, 110].

None of these issues are insuperable for a number of reasons, none of which can however be considered definitive, but are discussed in [99, 111–114].

⁴ a is the angular momentum J divided by the BH mass.

At the very least, one can infer that the topic of particle collision signatures near BH horizons merits further study. Specifically, several ways have been proposed for observing BH-boosted annihilations:

1. It has been shown that there are some unbound geodesics around the axis of rotation [115]. If the ergosphere were evenly populated with injection of annihilation debris, an increasing fraction of null geodesics are unbound in the limit of large and increasing a . To feed these would require that annihilation seeds the Penrose effect.
2. Penrose boosting of the energetics of collisional debris can occur in the ergosphere. Sufficiently detailed models have not been worked out however to come to a quantitative result [110, 116, 117].
3. There is no horizon near naked singularities. Dirty BH are another option. In these cases collisions at infinite CMS energies are possible [118].

Given the considerable interest should any signal be observable, and that the possibility of such an effect remains to be clarified, we have decided to explore a potentially unique signal from KK particle annihilations near the horizon. For our further considerations we stick for simplicity to the case of a non-rotating Schwarzschild BH. Because of the spherical symmetry of the system, it is enough to study the collision of DM particles in the equatorial plane to recover the general solution.

Considering the DM density around a BH, described by the spike and plateau configuration, a key scale ratio is that of plateau scale to Schwarzschild radius,

$$\frac{r_p}{r_S} = \left(\frac{c}{\sigma}\right)^2 \left(\frac{\langle\sigma v_{\text{rel}}\rangle t}{m_{\text{DM}}}\rho_{1/2}\right)^{1/\gamma'} \left(\frac{M_{1/2}}{M_{\text{BH}}}\right)^{\gamma/\gamma'}. \quad (20)$$

The plateau radius approaches the horizon for the most massive BHs: this amplifies the annihilation flux considerably.

The maximum luminosity (number of γ s per second) is evaluated at $r_h = 2r_S$,

$$L_h = \frac{4\pi}{3} \frac{(2r_S)^3}{\langle\sigma v_{\text{rel}}\rangle t^2}, \quad (21)$$

and the total spike luminosity is

$$L_{sp} = L_h \left(\frac{r_p}{2r_S}\right)^3. \quad (22)$$

This reduces to

$$L_{sp} = \left(\frac{c}{\sigma}\right)^6 \left(\frac{\langle\sigma v_{\text{rel}}\rangle t}{m_{\text{DM}}}\rho_{1/2}\right)^{3/\gamma'} \left(\frac{M_{1/2}}{M_{\text{BH}}}\right)^{3\gamma/\gamma'} \times \frac{32\pi}{3} \frac{r_S^3}{\langle\sigma v_{\text{rel}}\rangle t^2}. \quad (23)$$

For scaling purposes, we assume $\sigma^4 = G^2 \Sigma_{1/2} M_{1/2}$ and $\rho_{1/2} = \Sigma_{1/2}^{3/2} M_{1/2}^{-1/2}$, where $\Sigma_{1/2} = \rho_{1/2} r_{1/2}$. We assume σ is unchanged between r_{sp} and $r_{1/2}$. We now find

$$L_{sp} = \frac{32\pi}{3} \frac{\langle \sigma v_{\text{rel}} \rangle^{3/\gamma' - 1}}{m_{\text{DM}}^{\gamma/\gamma'}} t^{(3/\gamma' - 2)} \Sigma_{1/2}^{\frac{3}{2}(3/\gamma' - 1)} \times \left(\frac{M_{\text{BH}}}{M_{1/2}} \right)^{3(1 - \gamma/\gamma')} M_{1/2}^{\frac{3}{2}(1 - 1/\gamma')}. \quad (24)$$

Let us consider the case of a NFW halo profile: in the central region, $\gamma = 1$ and $\gamma' = 7/3$. Here we have

$$L_{sp} = \frac{32\pi}{3} \frac{\langle \sigma v_{\text{rel}} \rangle^{2/7}}{m_{\text{DM}}^{9/7}} t^{-5/7} \Sigma_{1/2}^{3/7} \left(\frac{M_{\text{BH}}}{M_{1/2}} \right)^{6/7} M_{\text{BH}}^{6/7}. \quad (25)$$

To get maximal enhancement the angular momenta should be opposite in sign, as shown in Fig. 6 in the left panel, where the DM rest mass is fixed to unity. The enhancement in the CMS energy decreases fast as soon as the angular momenta decrease or as soon as the distance from r_h increases (right panel). The Schwarzschild BH provides at most a CMS energy 4.5 times the DM mass. Such an acceleration is enough to excite the second and fourth KK levels, see Fig. 4, producing a pair of gamma ray lines. Potentially in the case of a Kerr BH the two gamma ray lines might become a line ‘forest’, because of the almost infinite CMS energy at disposal to the DM particles.

However each emitted photon will be subject to gravitational and Doppler redshift, which in principle depends on where the collisions occur and in which direction the photon is emitted. The photons are emitted close to the BH horizon with initial energy E_γ^0 and are boosted with the CMS velocity β of the annihilating DM particle pair. The gravitational redshift denotes the redshift in energy a photon undergoes when detected by an observer co-moving with the source, while the Doppler shift arises by moving to the reference frame of a distant observer at rest. The total redshift is thus given by

$$E_\gamma = E_\gamma^0 \sqrt{1 - \frac{r_S}{r}} \frac{\sqrt{1 - \beta^2}}{1 + v_{\text{tot}} \cos \delta}, \quad (27)$$

with δ being the angle at which the photon is emitted with respect to the velocity v_{tot} of the two DM particle system. We define a total mean redshift factor \bar{R}_{tot} to assess the smearing in the photon energy detected by a distant observer (the details are given in Appendix D), while the spectral feature is maintained, as discussed in Section III B. The total mean redshift factor is the average over all possible trajectories of the emitted photons

One can now see the explicit dependence on BH mass M_{BH} . The dependence on $M_{\text{BH}}/M_{1/2}$ is found to be constant at the present epoch (and to be reduced weakly with increasing redshift) [119]. The empirical dependence of surface brightness on galaxy luminosity, both defined at the effective radius (equivalent to a correlation between $\Sigma_{1/2}$ and $M_{1/2}$) is also weak [120].

Let us consider now two DM particles which, accelerated by the BH, collide and emit photons. The CMS energy depends on the distance r of the collision point from the BH horizon and on the angular momentum of the DM particles, l_1 and l_2 respectively, as in [52, 53]:

$$E_{\text{CM}}^2 = 2m_{\text{B}^{(1)}}^2 \frac{r^2(2r - r_S) - l_1 l_2(r - r_S) - \sqrt{r_S r^2 - l_1^2(r - r_S)} \sqrt{r_S r^2 - l_2^2(r - r_S)}}{r^2(r - r_S)}. \quad (26)$$

along the l.o.s. which escape the BH. The photon energy observed by the distant detector is then given by

$$E_\gamma = E_\gamma^0 \bar{R}(r)_{\text{tot}}, \quad (28)$$

while the initial injected spectrum becomes

$$\frac{dN_\gamma^f}{dE_\gamma^0} = \frac{dN_\gamma^f}{dE_\gamma} \frac{dE_\gamma}{dE_\gamma^0}. \quad (29)$$

Considering point sources, from Eq. (8) we can compute the photon flux observed at the Earth position from a SMBH at a distance D after having integrated over the solid angle

$$\frac{d\Phi}{dE_\gamma} = \frac{1}{2m_{\text{DM}}^2} \frac{1}{D^2} \times \int_{r_S}^{3/2r_S} r^2 \rho^2(r) \left\langle \sigma v_{\text{rel}} \sum_f B_f \frac{dN_\gamma}{dE_\gamma} \right\rangle dr, \quad (30)$$

where the upper limit of integration is given by the maximum value of r which can lead a E_{CMS} large enough to excite at least the first the resonance, as detailed in Appendix D. The GR effects that redshift the photons are given by Eqs. (28) and (29), which modify Eq. (13) into

$$\frac{d\Phi_{\text{res}}}{dE_\gamma} \simeq \frac{N_\gamma(\sigma v_{\text{rel}})_{\text{res}}}{4(\bar{R}(r_S)_{\text{tot}} E_\gamma^0)^3} \times \frac{\bar{R}(r_S)_{\text{tot}} \tilde{J}_{\text{line}}(\bar{R}(r_S)_{\text{tot}} E_\gamma^0) \Gamma_{\text{res}}^2 m_{\text{res}}^2}{(4\bar{R}(r_S)_{\text{tot}}^2 (E_\gamma^0)^2 - m_{\text{res}}^2)^2 + \Gamma_{\text{res}}^2 m_{\text{res}}^2}, \quad (31)$$

with

$$\tilde{J}_{\text{line}}(\bar{R}(r_S)_{\text{tot}} E_\gamma^0) \equiv \frac{1}{D^2} \frac{m_{\text{DM}}^2}{t_{\text{BH}}^2 (\sigma v_{\text{rel}})^2} \times \int_{r_S}^{3/2r_S} dr r^2 \frac{p_{r,\text{rel}}(v_{\text{rel}})}{v_{\text{rel}}/4}. \quad (32)$$

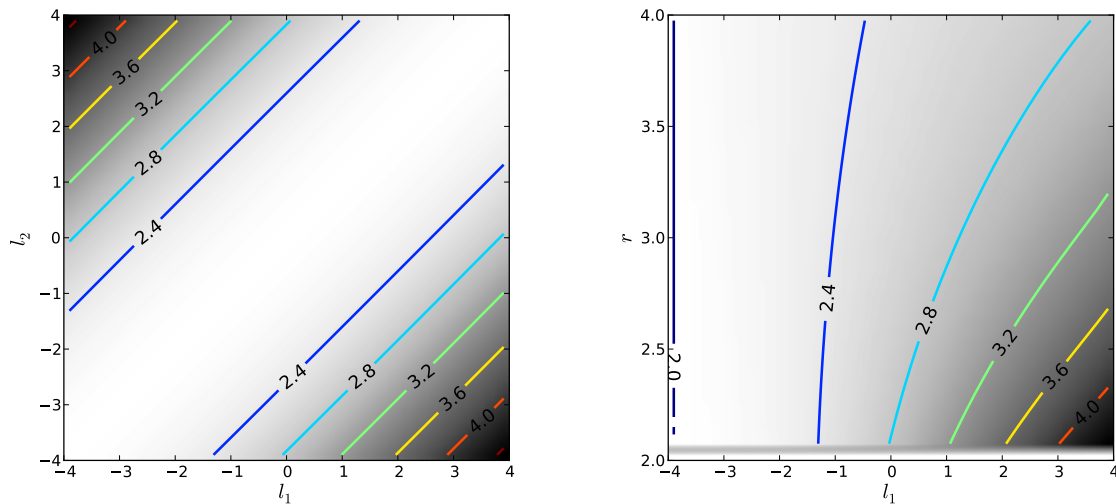


FIG. 6. Left: Contour plot of the CMS energy per unit DM rest mass as a function of the two DM angular momenta l_1 and l_2 , with the collision radial coordinate being fixed at $r = r_S$. Right: Same as left as a function of the collision radial coordinate r and the angular momentum of the first DM particle l_1 , with l_2 fixed at its minimal value ($l_2 = -4$).

Here we used the explicit formula for the density spike, Eq. (18); notice that there is no more r dependence for the density profile as the region of interest for the signal is contained within the plateau region. The velocity distribution is simply given by gravitational motion around the BH and it is typically of the order of c , which we take as reference value. There are several astrophysical factors that affect the observed flux:

1. The mean total redshift decreases the observed photon energy. In fact, simple energy conservation arguments imply that the maximally observable energy for a distant observer still corresponds to the rest mass of the annihilating DM particles (unless very efficient Penrose boosting is at place);
2. In general, redshift and Doppler effects will also broaden the line signal considerably. The intrinsic width of the signal is much smaller than the experimental resolution, however, so we do not expect this to significantly affect observational prospects;
3. The distance of the SMBH tends to decrease the flux, while its Schwarzschild radius boosts the signal: supergiant BHs can compensate with their mass their distance and perform better for instance than SagA*, as it will be discussed below;
4. The time of BH formation is also relevant, as shorter t_{BH} lead to larger fluxes;
5. The value of the annihilation cross-section in the early universe is fixed by the scaling relation in Eq. (7) and corresponds to $\sigma v_{rel} \simeq 1.3 \times 10^{-26} \text{cm}^3/\text{s}$ for a 1.2 TeV KK particle;
6. The $p_{r,rel}(v_{rel})$ term, which accounts for the probability that the two DM particles have opposite

and maximal angular momentum, in order to collide with a CMS energy large enough to excite the resonance. The solutions of the geodesics equations for massive particle would require numerical simulation. Assuming that the DM rest mass is negligible with respect to the CMS energy [55] the geodesics can be approximated with those of massless objects, concluding that the infall of particles is not radial unless at the exact position $r = r_S$. The infall orbits are even more complicated and far from the radial behavior in the Kerr geometry [57, 121]. In light of these uncertainties, we simply set $p_{r,rel}(v_{rel})/v_{rel}/4$ to unity in our estimation of the photon flux near the resonances – keeping in mind that a full treatment, which is beyond the scope of this work, might turn out to yield a significantly smaller value.

We roughly estimate the expected gamma ray flux at the Earth position for two SMBHs using Eq. (31), with $m_{B(1)} = 1.2 \text{ TeV}$ and for the first peak produced by the $H^{(2)}$ resonance, which is the dominant one.

a. SMBH in the GC The center of the Milky Way hosts a SMBH with $\simeq 4.6 \times 10^6 M_\odot$, which corresponds to a Schwarzschild radius of about $4 \times 10^{-7} \text{ pc}$. For a density plateau of the order of $10^{11} M_\odot/\text{pc}^3$, derived considering a SMBH formation time of 10^8 yr , the flux near the resonance is $\Phi_{res} \sim 10^{-18} \text{ photons/cm}^2/\text{s}$, which is slightly below the reach of HESS or CTA for line searches.

b. Supergiant elliptical galaxy M87 The case of the Virgo A galaxy is more promising for observation, because it hosts a supergiant BH, $M_{BH} = 6.6 \times 10^9 M_\odot$. This increases considerably the Schwarzschild radius $r_S \sim 6 \times 10^{-4} \text{ pc}$, which in turn compensates the fact that the SMBH is much more distant than the GC, i.e. $D = 16.4 \text{ Mpc}$. In total this provides a boost of $\sim 10^3$ to the gamma ray flux with respect to the case of SagA*,

$\Phi_{\text{res}} \sim 10^{-15}$ photons/cm²/s which might be observable by the next generation of gamma ray telescopes.

VII. CONCLUSIONS

In this article, we have demonstrated that taking into account the non-vanishing velocities of annihilating DM particles can significantly change the predictions for the signal expected in indirect DM searches. This is especially true for Kaluza-Klein DM, where resonances naturally appear close to the CMS energy in the zero-velocity limit. For our concrete calculations we have focussed on a class of rather popular UED models, where the DM particle is given by the first KK excitation of the photon, but the general features we have discussed are generic to most KK DM models. In particular, we have pointed out the remarkable fact that these resonances can rather generically enhance line signals significantly more than the continuum gamma ray spectrum from DM annihilation. This has important phenomenological implications for the search for TeV-scale DM candidates with upcoming instruments like CTA.

For the model that we have chosen to investigate we have presented a systematic discussion of the dominant processes, for which we performed detailed higher-order computations to update existing results for the zero-velocity limit. This included hitherto neglected diagrams and a set of rather complex computations of various radiatively generated couplings (as explained in detail in the technical Appendices). In the specific case of the rather restrictive mUED model, and for typical galactic velocities, those new contributions only increase the monochromatic photon flux by $\mathcal{O}(10\%)$; for more general models, however, the line signal may indeed be enhanced by up to about 3 orders of magnitude.

Large enhancements of the line signals can also be found in astrophysical environments where DM velocities larger than $\sim 0.01c$ prevail. A particularly interesting place to look for line signals from DM annihilation are thus SMBHs like in the center of our galaxy. In this case, in fact, one may even encounter CMS energies several times the DM rest mass. For such a situation, we have identified a new 'smoking gun' signature that consists of several equally spaced gamma ray lines and that would unequivocally point to the extra-dimensional origin of the annihilation signal. While a very rough estimate for the expected fluxes seems to indicate that rather favorable assumptions about the astrophysical environment are needed to observe such a multi-line signal, a full investigation is beyond the scope of this work. Given the potentially spectacular signature, however, it is certainly worthwhile to further explore this exciting possibility.

ACKNOWLEDGMENTS

TB acknowledges support from the German Research Foundation (DFG) through the Emmy Noether grant BR 3954/1-1. The research of CA and JS has been supported at IAP by the ERC project 267117 (DARK) hosted by Université Pierre et Marie Curie - Paris 6, PI J. Silk. JS acknowledges the support of the JHU by NSF grant OIA-1124403, while CA acknowledges the partial support of the European Research Council through the ERC starting grant *WIMPs Kairos*, PI G. Bertone. MV acknowledges support from the Forschungs- und Wissenschaftsstiftung Hamburg through the program "Astroparticle Physics with Multiple Messengers". For the computation and numerical evaluation of the relevant Feynman diagrams we largely relied on FeynCalc [122] and LoopTools [123].

Appendix A: Decay widths of second-KK-level particles

As discussed in Section III B, the way resonances decay has phenomenological consequences that are essential to our analysis. In this Appendix, we provide technical details about the computation of the relevant decay widths of potentially resonant KK particles, c.f. Fig. 1 and Tab. I. For concreteness, we will fix

$$\Lambda R = 5, \quad R^{-1} = 1.2 \text{ TeV} \quad (\text{A1})$$

whenever we state numerical results.

While tree-level couplings preserve KK number and straightforwardly follow from the SM Lagrangian in 5D (see, e.g., Refs. [124, 125] for a list of Feynman rules), the KK-number violating effective couplings that one encounters in resonant diagrams require a considerably more involved treatment. The general formalism to obtain these effective vertices, which have to be renormalized by counterterms located on the brane, is detailed in Ref. [21]; it involves not only the calculation of radiative corrections to the vertex on the brane but also, at the same one-loop order, kinetic and mass mixing effects between states of different KK number. Here, we will in particular make use of the result that for the coupling of a generic gauge field A_μ to chiral SM fermions f ,

$$\mathcal{L}_{\text{eff}} \supset g_{\text{eff}}^{A\bar{f}f} A_\mu^{(2)} \bar{f}^{(0)} \gamma^\nu T^a \frac{1 \pm \gamma^5}{2} f^{(0)}, \quad (\text{A2})$$

the coupling constant for the corresponding vertex in the mUED case is given by

$$g_{\text{eff}}^{A\bar{f}f} = \frac{g}{\sqrt{2}} \left[\frac{\bar{\delta}(m_{A^{(2)}}^2)}{m_2^2} - 2 \frac{\bar{\delta}(m_{f^{(2)}})}{m_2} \right], \quad (\text{A3})$$

where g is the corresponding coupling between zero modes, $m_n \equiv n/R$ and $\bar{\delta}(m)$ refers to radiative mass corrections due to terms localized on the brane.

1. $B^{(2)}$ decay

In the mUED model the $B^{(2)}$ is the lightest of all level-2 KK particles, its mass being almost unaffected by radiative corrections. Kinematically, the only possible decay is directly into SM particles by means of KK-number violating effective vertices and its leading decay channel is $B^{(2)} \rightarrow \bar{q}q$ with a branching ratio of around 99% [74].

The mass corrections of $B^{(2)}$ and $f_{s,d}^{(1)}$ are given by [21, 74]

$$\frac{\bar{\delta}m_{B^{(2)}}^2}{m_2^2} = -\frac{g'^2}{6} \frac{\log \frac{\Lambda^2}{\mu^2}}{16\pi^2}, \quad (\text{A4})$$

$$\frac{\bar{\delta}m_{f_s^{(1)}}}{m_2} = \left(\frac{9}{4} Y_{f_s}^2 g'^2 + 3g_s^2 - \frac{3}{2} y_f^2 \right) \frac{\log \frac{\Lambda^2}{\mu^2}}{16\pi^2}, \quad (\text{A5})$$

$$\frac{\bar{\delta}m_{f_d^{(1)}}}{m_2} = \left(\frac{9}{4} Y_{f_d}^2 g'^2 + \frac{27}{16} g^2 + 3g_s^2 - \frac{3}{4} y_f^2 \right) \frac{\log \frac{\Lambda^2}{\mu^2}}{16\pi^2}, \quad (\text{A6})$$

where Y refers to the hypercharge, g' [g] denotes the $U(1)$ [$SU(2)$] coupling constant and y the Yukawa coupling. The term proportional to the strong coupling constant g_s only appears for quarks. Using Eq. (A3), this translates into the vertex relevant for $B^{(2)} \rightarrow \bar{f}f$ (as reported in Ref. [74])

$$\mathcal{L}_{\text{eff}} \supset -\bar{f} \gamma^\mu \left(g_{\text{eff}}^L \frac{1 - \gamma^5}{2} + g_{\text{eff}}^R \frac{1 + \gamma^5}{2} \right) f B_\mu^{(2)}, \quad (\text{A7})$$

$$g_{\text{eff}}^L = \frac{g' Y_{f_d}}{\sqrt{2}} \left[\frac{g'^2}{6} (1 + 27 Y_{f_d}^2) + \frac{27}{8} g^2 + 6g_s^2 - \frac{3}{2} y_f^2 \right] \frac{\log \frac{\Lambda^2}{\mu^2}}{16\pi^2}, \quad (\text{A8})$$

$$g_{\text{eff}}^R = \frac{g' Y_{f_s}}{\sqrt{2}} \left[\frac{g'^2}{6} (1 + 27 Y_{f_s}^2) + 6g_s^2 - 3y_f^2 \right] \frac{\log \frac{\Lambda^2}{\mu^2}}{16\pi^2}. \quad (\text{A9})$$

The decay rate then follows straight-forwardly as

$$\frac{\Gamma_{B^{(2)} \rightarrow \bar{f}f}}{m_{B^{(2)}}} = \frac{1}{12\pi} \left(1 - \frac{4m_f^2}{m_{B^{(2)}}^2} \right)^{\frac{1}{2}} \times \left[\left(1 + \frac{2m_f^2}{m_{B^{(2)}}^2} \right) g_V^2 + \left(1 - \frac{4m_f^2}{m_{B^{(2)}}^2} \right) g_A^2 \right], \quad (\text{A10})$$

where $g_V \equiv (g_{\text{eff}}^R + g_{\text{eff}}^L)/2$ and $g_A \equiv (g_{\text{eff}}^R - g_{\text{eff}}^L)/2$. Adopting Eq. (A1), the above evaluates numerically to $g_{\text{eff}}^L = 0.09$ and $g_{\text{eff}}^R = 0.11$, implying a decay rate of $\Gamma_{B^{(2)}} \approx 0.813 \text{ GeV}$.

When allowing for arbitrary mass splittings on the other hand, as possible in generic UED scenarios, $B^{(2)}$ would instead mainly decay into a pair of first-KK-level charged leptons; the corresponding rate is then given by

$$\frac{\Gamma_{B^{(2)} \rightarrow \bar{l}_s^{(1)} l_s^{(1)}}}{m_{B^{(2)}}} = \frac{Y_{l_s}^2 g'^2}{4\pi} \left(1 - \frac{4m_{l_s^{(1)}}^2}{m_{B^{(2)}}^2} \right)^{\frac{1}{2}} \left(1 + \frac{2m_{l_s^{(1)}}^2}{m_{B^{(2)}}^2} \right). \quad (\text{A11})$$

In this case, the existence of a tree-level rather than loop-suppressed coupling typically over-compensates the additional phase-space suppression, and the decay happens considerably faster (with $\Gamma \sim 10 \text{ GeV}$).

2. $A_3^{(2)}$ decay

In the mUED model, $A_3^{(2)}$ is considerable more massive than $B^{(2)}$. As a result, kinematics allows for six

different decay channels into first-level leptons $\bar{\ell}_{s,d}^{(1)}\ell_{s,d}^{(1)}$, which dominates over the only other possible tree-level decay channels into first-KK-level scalar pairs. The corresponding decay rate is described by Eq. (A11), with $Yg' \rightarrow g/\sqrt{2}$. Adopting Eq. (A1), the total decay rate is well approximated by $\Gamma_{A_3^{(2)}} \approx 70$ GeV.

In non-minimal scenarios, mass splittings may kinematically not allow the $A_3^{(2)}$ to decay into first-KK-level states, but only into SM particles. Assuming that non-trivial mass and kinetic boundary terms are added at the cut-off scale, in analogy to Eq. (A7), the radiative vertex that couples $A_3^{(2)}$ to SM fermion is given by

$$\mathcal{L}_{\text{eff}} \supset -g_{\text{eff}}^L \bar{f} \gamma^\mu \frac{1 - \gamma_5}{2} f A_{3\mu}^{(2)}, \quad (\text{A12})$$

$$g_{\text{eff}}^L = \frac{gT_{3f}}{\sqrt{2}} \left[\frac{9Y_{fL}^2}{2} g'^2 - \frac{33}{8} g^2 + 6g_s^2 - \frac{3}{2} y_f^2 \right] \frac{\log \frac{\Lambda^2}{\mu^2}}{16\pi^2}, \quad (\text{A13})$$

where T_{3f} is the fermion weak isospin charge. In deriving this, we used again formula (A3) and also [21]

$$\frac{\bar{\delta} m_{W^{(2)}}^2}{m_2^2} = \frac{15}{2} \frac{g^2}{16\pi^2} \log \frac{\Lambda^2}{\mu^2}. \quad (\text{A14})$$

The decay rate is then calculated just like in Eq. (A10). Numerically, the total width becomes $\Gamma_{A_3^{(2)}} \approx 0.8$ GeV, with branching ratios of 11.2% for $\bar{t}t$, 11.4% for $\bar{b}b$, 18.0% for other quark-antiquark pairs and 0.9% for every lepton pair.

3. $H^{(2)}$ decay

In the mUED model the only possible tree-level decay of the second KK-level Higgs, $H^{(2)} \rightarrow a_0^{(1)} B^{(1)}$, becomes kinematically forbidden for $R^{-1} \lesssim 1$ TeV. Therefore, $H^{(2)}$ is also metastable and decays predominantly into top anti-top pairs due to a radiatively generated vertex $\mathcal{L}_{\text{eff}} \supset g_{\text{eff}} H^{(2)} \bar{t}t$, where (λ_h being the quartic coupling of the Higgs potential) [74]⁵

$$g_{\text{eff}} = \frac{y_t}{12} \left[16g_s^2 + \frac{33}{4} g^2 + \frac{23}{6} g'^2 - 9y_t^2 + 3\lambda_h \right] \frac{\log \frac{\Lambda^2}{\mu^2}}{16\pi^2}.$$

From this, the decay rate follows as

$$\frac{\Gamma_{H^{(2)} \rightarrow \bar{t}t}}{m_{H^{(2)}}} = \frac{3g_{\text{eff}}^2}{8\pi} \left(1 - \frac{4m_t^2}{m_{H^{(2)}}^2} \right)^{\frac{3}{2}}.$$

The factor 3 accounts for the number of colors. Numerically, adopting Eq. (A1), we find $g_{\text{eff}} = 0.0189$ and thus

⁵ Here, we corrected a similar formula found in [74] by including scalar-vector-fermion loops. See appendix C for more details.

a decay rate of $\Gamma_{H^{(2)}} \approx 99.7$ MeV. Note that the decay of $H^{(2)}$ in SM gauge bosons is suppressed by a factor of roughly $\frac{1}{3}(m_W/m_t)^2 \sim \mathcal{O}(0.1)$. The decay into a $B^{(1)}$ pair, finally, is the only allowed decay channel into KK excitations in the mUED scenario (c.f. Fig. 2). Due to the small mass splitting, however, this channel contributes at an even lower rate (with $\Gamma_{H^{(2)}} \approx 2.4$ MeV).

Equipping the $H^{(2)}$ with a sufficiently large mass in non-minimal scenarios, on the other hand, it will mainly decay into $\bar{t}_s^{(1)} t_d^{(1)}$ and $\bar{t}_d^{(1)} t_s^{(1)}$ pairs. In this case, one has an *axial* scalar coupling with

$$g_{\text{eff}} = 2g \frac{m_f}{m_W}. \quad (\text{A15})$$

Numerically, this gives $\Gamma_{H^{(2)}} \sim 160$ GeV, i.e. a much faster decay than in the mUED scenario.

Appendix B: Resonant LKP annihilation amplitudes

In this Appendix, we provide technical details about the computation of the full amplitudes that describe the resonant annihilation of LKP pairs. The Feynman diagrams of Fig. 1 can compactly be written as

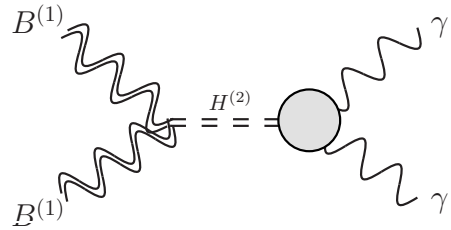
$$i\mathcal{A}_V = \epsilon_1^\mu \epsilon_2^\nu L_{V\mu\nu} \frac{-\eta_{\rho\sigma} + \frac{P_\rho P_\sigma}{M_V^2}}{s - M_V^2 + iM_V \Gamma_V} R_{V\alpha}^\sigma \epsilon_\gamma^\alpha, \quad (\text{B1})$$

$$i\mathcal{A}_S = \epsilon_1^\mu \epsilon_2^\nu L_{S\mu\nu} \frac{1}{s - M_S^2 + iM_S \Gamma_S} R_{S\alpha\beta} \epsilon_\gamma^\alpha \epsilon_Z^\beta, \quad (\text{B2})$$

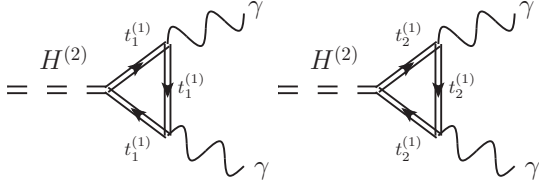
where V and S stand for vector ($B^{(2)}$, $A_3^{(2)}$) and scalar ($H^{(2)}$, $a_0^{(2)}$) resonances respectively. The tensors $L_{V,S}$, $R_{V,S}$ encode therefore the physical information of the left and right blobs in each diagram of Fig. 1. In the following, we will focus our discussion of these tensors in a final-state-to-final-state basis.

1. $B^{(1)} B^{(1)} \rightarrow \gamma\gamma$

The relevant Feynman diagram that contributes to this process is



Here, $L_{\mu\nu} = ig_{B^{(1)} B^{(1)} H^{(2)}} \eta_{\mu\nu} = i(g'^2 v/2) \eta_{\mu\nu}$, where v is the vacuum expectation value of the Higgs field and the blob on the right-hand-side represents the superposition of several triangle diagrams, the leading ones being



Decomposing the corresponding loop-integrals in terms of Passarino-Veltman functions [126] yields (in the limit where both KK top quarks have the same mass)

$$R_{H^{(2)}\alpha\beta}^{\gamma\gamma} = -\frac{\alpha_{\text{em}} Q_t^2}{\pi} \frac{4igm_t \sin 2\alpha_t^{(1)}}{m_W} \frac{m_{t^{(1)}}}{s} \quad (\text{B3})$$

$$\left(\left[2 - (s - 4m_{t^{(1)}}^2) C_0(0, 0, s, m_{t^{(1)}}^2, m_{t^{(1)}}^2, m_{t^{(1)}}^2) \right] \right. \\ \times [s\eta_{\alpha\beta} - 2k_{1\alpha}k_{2\beta} - 2k_{1\beta}k_{2\alpha}] \\ \left. - 4 \left[2B_0(s, m_{t^{(1)}}^2, m_{t^{(1)}}^2) - 2B_0(0, m_{t^{(1)}}^2, m_{t^{(1)}}^2) \right. \right. \\ \left. \left. + s C_0(0, 0, s, m_{t^{(1)}}^2, m_{t^{(1)}}^2, m_{t^{(1)}}^2) \right] k_{1\alpha}k_{2\beta} \right).$$

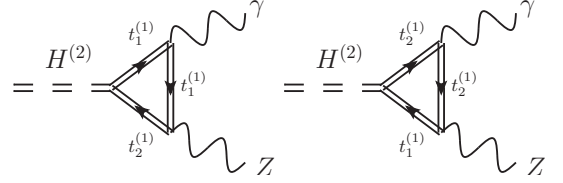
Here, k_1 and k_2 are the outgoing momenta and $s = (k_1 + k_2)^2$, $\alpha_e m \approx 1/128$ is the fine-structure constant at the TeV scale and $Q_t = 2/3$ is the charge of the top-quark. The angle $\alpha^{(1)}$ describes the mixing between first KK-level flavour and mass eigenstates; in the mUED case, this is only significantly different from zero for the case of top quarks (with $\alpha_t^{(1)} \approx 0.071$). Notice that

$R_{H^{(2)}\alpha\beta}$ manifestly satisfies the Ward identities both here and for the amplitudes presented further down, namely $k_1^\alpha R_{H^{(2)}\alpha\beta} = k_2^\beta R_{H^{(2)}\alpha\beta} = 0$.

Concerning a possible contribution from the $a_0^{(2)}$ resonance, we note that $ig_{B^{(1)}B^{(1)}a_0^{(2)}} = 0$ at tree level and, more importantly, $\Gamma_{a_0^{(2)} \rightarrow \gamma\gamma, \gamma Z} = 0$. The latter can be traced back to the absence of anomalous three-gauge-boson couplings in the full theory (recall that a_0 contains the higher-dimensional component of the Z boson).

2. $B^{(1)}B^{(1)} \rightarrow Z\gamma$

Most of the conclusions from the last section can also be drawn for this process. The main difference is that the Z boson is massive and has not only vector, but also axial-vector couplings. The following two diagrams thus need in principle to be added for the computation of $R_{\alpha\beta}$ in this case, but cancel in the limit of $m_{t^{(1)}} = m_{t_2^{(1)}}$:



In total, we find

$$R_{H^{(2)}\alpha\beta}^{\gamma Z} = -\frac{egQ_t}{\pi^2 \cos \theta_W} \frac{igm_t}{m_W} \frac{m_{t^{(1)}} \sin 2\alpha_t^{(1)}}{s - m_Z^2} \left(B [(s - m_Z^2)\eta_{\alpha\beta} - 2k_{1\beta}k_{2\alpha}] + C [k_{2\beta} - \frac{2m_Z^2}{s - m_Z^2} k_{1\beta}] k_{1\alpha} \right) \quad (\text{B4})$$

with

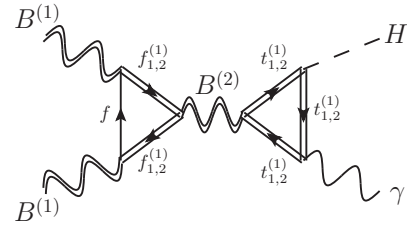
$$B = \left(Y_{t_L} \sin^2 \theta_W - \frac{1}{4} \cos 2\theta_W \right) \left[2 - (s - m_Z^2 - 4m_{t^{(1)}}^2) C_0(0, m_Z^2, s, m_{t^{(1)}}^2, m_{t^{(1)}}^2, m_{t^{(1)}}^2) - \right. \\ \left. - \frac{2m_Z^2}{s - m_Z^2} [B_0(s, m_{t^{(1)}}^2, m_{t^{(1)}}^2) - B_0(m_Z^2, m_{t^{(1)}}^2, m_{t^{(1)}}^2)] \right] \quad (\text{B5})$$

$$C = 2 \left(Y_{t_L} \sin^2 \theta_W - \frac{1}{4} \cos 2\theta_W \right) \left[2 + (s + m_Z^2 + 4m_{t^{(1)}}^2) C_0(0, m_Z^2, s, m_{t^{(1)}}^2, m_{t^{(1)}}^2, m_{t^{(1)}}^2) \right] \quad (\text{B6})$$

$$+ 2 \frac{2s + m_Z^2}{s - m_Z^2} B_0(s, m_{t^{(1)}}^2, m_{t^{(1)}}^2) - 2 \frac{s + 2m_Z^2}{s - m_Z^2} B_0(m_Z^2, m_{t^{(1)}}^2, m_{t^{(1)}}^2) - 2B_0(0, m_{t^{(1)}}^2, m_{t^{(1)}}^2) \quad (\text{B7})$$

3. $B^{(1)}B^{(1)} \rightarrow H\gamma$

In this case, the relevant Feynman diagrams are given by



where the vector resonance $B^{(2)}$ can also be interchanged with $A_3^{(2)}$. The reason that top quark contributions dom-

inate in the tensor R_V is, as in the cases discussed so far, simply given by the presence of a Yukawa. For L_V , on the other hand, this follows from anomaly cancellation in the SM: $\sum_f L_{f\mu\nu}^{\rho}|_{m_f \rightarrow 0} \propto \sum_f (Y_R^3 + Y_L^3) = 0$ implies that

$L_{\mu\nu}^{\rho} = \sum_f L_{f\mu\nu}^{\rho} \simeq L_{\text{top}\mu\nu}^{\rho} - L_{\text{top}\mu\nu}^{\rho}|_{m_t \rightarrow 0}$ (with the sum running over all SM fermions f). While this results in an expression for $L_{\mu\nu}^{\rho}$ that is too lengthy to be displayed here, the tensor $R_{B^{(2)}\alpha\beta}^{\gamma H}$ takes a very similar form as in the previous case:

$$R_{B^{(2)}\alpha\beta}^{\gamma H} = -\frac{eg'Q_t(Y_{t_L} + Y_{t_R})}{2\pi^2} \frac{igm_t}{m_W} \frac{m_{t(1)} \sin 2\alpha_t^{(1)}}{(s - m_H^2)^3} \left(B[(s - m_H^2)\eta_{\alpha\beta} - 2k_{1\beta}k_{2\alpha}] + [C_2k_{2\beta} - C_1k_{1\beta}]k_{1\alpha} \right) \quad (\text{B8})$$

with

$$B = (s - m_H^2) \left([2 + (s - m_H^2 + 4m_{t(1)}^2)C_0(0, m_H^2, s, m_{t(1)}^2, m_{t(1)}^2, m_{t(1)}^2)](s - m_H^2) \right. \quad (\text{B9})$$

$$\left. - 2s[B_0(s, m_{t(1)}^2, m_{t(1)}^2) - B_0(m_H^2, m_{t(1)}^2, m_{t(1)}^2)] \right)$$

$$C_2 = -2(s - m_H^2) \left[(s - m_H^2)[2 + (s + m_H^2 + 4m_{t(1)}^2)C_0(0, m_H^2, s, m_{t(1)}^2, m_{t(1)}^2, m_{t(1)}^2)] + 2(s + 2m_H^2)[B_0(s, m_{t(1)}^2, m_{t(1)}^2) \right. \\ \left. - B_0(m_H^2, m_{t(1)}^2, m_{t(1)}^2)] + 2(s - m_H^2)[B_0(s, m_{t(1)}^2, m_{t(1)}^2) - B_0(m_{t(1)}^2, m_{t(1)}^2, m_{t(1)}^2)] \right]$$

$$C_1 = 4[m_H^2(s - m_H^2)[2 + (s + 2m_{t(1)}^2)C_0(0, m_H^2, s, m_{t(1)}^2, m_{t(1)}^2, m_{t(1)}^2)] + 2m_H^2(2s + m_H^2)[B_0(s, m_{t(1)}^2, m_{t(1)}^2) \\ - B_0(m_H^2, m_{t(1)}^2, m_{t(1)}^2)] + (s^2 - m_H^4)[B_0(s, m_{t(1)}^2, m_{t(1)}^2) - B_0(m_{t(1)}^2, m_{t(1)}^2, m_{t(1)}^2)].$$

For $R_{A_3^{(2)}\alpha\beta}^{\gamma H}$, one simply needs to replace $\sin 2\alpha_t^{(1)}(Y_{t_L} + Y_{t_R})$ in Eq. (B8) with $(1/4)\sin 4\alpha_t^{(1)}$.

The mixing terms, on the other hand, are given by

$$\delta\mathcal{L} \supset L \left(\frac{\delta(x_5) + \delta(x_5 - L)}{2} \right) \frac{1}{64\pi^2} \log \frac{\Lambda^2}{\mu^2} \times \\ \times [b_1^{s,d} \bar{t}_{s,d} i \not{\partial} t_{s,d;+,-} + b_2^{s,d} (\bar{t}_{s,d} \overleftarrow{\partial}_5 t_{s,d;+,-} + \\ + \bar{t}_{s,d;+,-} \partial_5 t_{s,d}) + c_1 \frac{1}{2} (\partial_\mu H)^2 + c_2 \frac{1}{2} H \partial_5^2 H], \quad (\text{C2})$$

Appendix C: $H^{(2k)}$ resonances

Similar to $H^{(2)}$, higher order scalar modes decay via KK-number violating processes in minimal scenarios. However, these decays occur with non-trivial branching ratios because, as the KK-mode increases, more and more final states start to become kinematically available. Therefore a careful analysis of the effective brane vertices describing such decays is needed. Fortunately, we can derive all of them from the master 5D vertex and from the kinetic and mass radiative mixing terms [21]. In Feynman gauge, the Vertex reads

$$\delta\mathcal{L}_{\text{eff}} = L^{3/2} \left(\frac{\delta(x_5) + \delta(x_5 - L)}{2} \right) \frac{y_t}{\sqrt{2}} \frac{1}{64\pi^2} \log \frac{\Lambda^2}{\mu^2} \times \\ \times \left[f_R H \bar{t}_d \frac{1 + \gamma_5}{2} t_s + f_L H \bar{t}_d \frac{1 - \gamma_5}{2} t_s + \text{h.c.} \right], \quad (\text{C1})$$

where x_5 is the fifth space coordinate, $L = \pi R$ is the length separating the orbifold fixed points and $f_{L,R}$ are given by

$$f_R = 8g_s^2 - \frac{3}{2}g^2 - \frac{1}{6}g'^2, \\ f_L = -2y_t(y_t + y_b) \approx -2y_t^2,$$

where the fields $(1 \pm \gamma_5)t/2$ are represented as t_{\pm} , and $b_{1,2}^{s,d}$ and $c_{1,2}$ are given by [21]

$$b_1^s = \frac{4}{3}g_s^2 + Y_{t_R}^2 g'^2 + 2y_t^2, \quad (\text{C3})$$

$$b_1^d = \frac{4}{3}g_s^2 + \frac{3}{4}g^2 + Y_{t_L}^2 g'^2 + y_t^2, \quad (\text{C4})$$

$$b_2^s = 5 \left(\frac{4}{3}g_s^2 + Y_{t_R}^2 g'^2 \right) - 2y_t^2, \quad (\text{C5})$$

$$b_2^d = 5 \left(\frac{4}{3}g_s^2 + \frac{3}{4}g^2 + Y_{t_L}^2 g'^2 \right) - y_t^2, \quad (\text{C6})$$

$$c_1 = -g'^2 - 2g^2, \quad (\text{C7})$$

$$c_2 = \frac{1}{2}g'^2 + g^2 - 2\lambda_h. \quad (\text{C8})$$

1. $H^{(4)}$ decay

The computation of decay rates for $H^{(2k)}$ in the minimal scenario follows from similar procedures as the corresponding calculation for $H^{(4)}$. Here we therefore compute this decay rate as an example.

Notice that the main difference between the life-times of $H^{(2)}$ and $H^{(4)}$ is that whereas the former decays with branching ratio ~ 1 into top quark-antiquark pairs,

the latter can decay into several states with comparable branching ratios. Namely, $H^{(4)} \rightarrow \bar{t}_s^{(1)} t_d^{(1)} (\bar{t}_d^{(1)} t_s^{(1)})$, $\bar{t}_{s,d}^{(2)} t^{(0)} (\bar{t}^{(0)} t_{s,d}^{(2)})$ and $\bar{t}t$ turn out to be the 7 dominant decay channels, where for instance the decays $H^{(4)} \rightarrow \bar{t}_{s,d}^{(1)} t_{d,s}^{(1)}$ are induced by the effective vertex

$$\delta\mathcal{L} \supset \frac{y_t}{64\pi^2} \log \frac{\Lambda^2}{\mu^2} H^{(4)} \left[\left(\frac{154}{9} g_s^2 + \frac{41}{16} g^2 + \frac{697}{432} g'^2 - \frac{23}{4} y_t^2 + \frac{8}{3} \lambda_h \right) \bar{t}_s^{(1)} t_d^{(1)} + \left(\frac{69}{9} g_s^2 - \frac{29}{16} g^2 - \frac{157}{432} g'^2 + \frac{3}{4} y_t^2 \right) \bar{t}_s^{(1)} \gamma_5 t_d^{(1)} + \text{h.c.} \right],$$

which is obtained by decomposing (C1) in terms of the KK modes and including the kinetic and mass mixing terms with $t_{s,d}^{(3)}$, $t_{s,d}^{(5)}$, $H^{(0)}$ and $H^{(2)}$. The numerical value for the total decay rate of $H^{(4)}$ amounts to $\Gamma_{H^{(4)}} = 3.1 \text{ GeV}$ when $\Lambda = 5/R$.

2. $B^{(1)} B^{(1)} H^{(2k)}$ effective vertices

In section B 1 we exploited the fact that EW-symmetry breaking provides us with a tree-level $B^{(1)} B^{(1)} H^{(2)}$ coupling when obtaining the $B^{(1)} B^{(1)} \rightarrow \gamma\gamma(\gamma Z)$ annihilation rates. Such a coupling does not exist for, say, $B^{(1)} B^{(1)} H^{(4)}$ in the classical theory since it violates KK-number symmetry. However, the same arguments from the previous section apply here and we find couplings of this kind at the loop-quantum level which are localized at the fixed points of the orbifold.

To obtain these effective vertices, we shall just as previously consider the master 5D radiative terms

$$\delta\mathcal{L} \supset L \left(\frac{\delta(x_5) + \delta(x_5 - L)}{2} \right) \frac{g'^2 v}{2} \frac{f_S}{64\pi^2} \log \frac{\Lambda^2}{\mu^2} H B_\mu B^\mu \quad (\text{C9})$$

and the kinetic and mass mixing terms

$$\delta\mathcal{L} \supset L \left(\frac{\delta(x_5) + \delta(x_5 - L)}{2} \right) \frac{1}{64\pi^2} \log \frac{\Lambda^2}{\mu^2} \left[-a_1^B \frac{1}{4} B_{\mu\nu} B^{\mu\nu} - a_2^B \frac{1}{2} (B_\mu \partial_5^2 B^\mu) + c_1 \frac{1}{2} (\partial_\mu H)^2 + c_2 \frac{1}{2} H \partial_5^2 H \right]. \quad (\text{C10})$$

The coefficients in the previous expression have already been computed in Ref. [21], while the coefficient f_S in (C9) can easily be computed by isolating the divergent terms of the Feynman diagrams in Fig. 7 and adding them up. In the Feynman gauge the result reads

$$f_S = \frac{3}{4} g'^2 + \frac{9}{4} g^2 + 12\lambda_h. \quad (\text{C11})$$

To check the correctness of this result, one can obtain the corresponding effective vertices and mixing terms

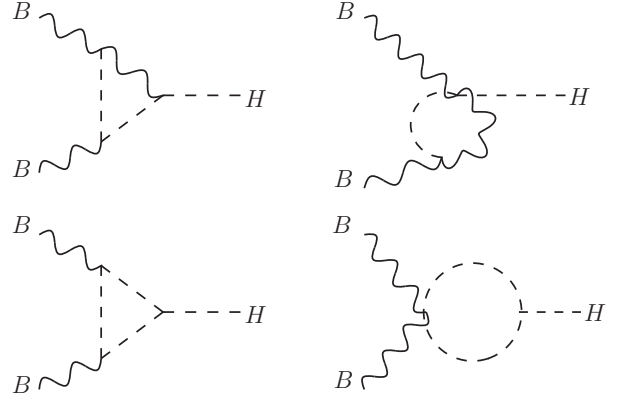


FIG. 7. Divergent Feynman diagrams participating in eq. (C9). Additional diagrams are obtained by charge conjugation or leg exchange of the initial B 's. Particles running on the loops include (correspondingly) all vector bosons and all scalars. Notice that there are no fermion loops since H couples to mixed doublet and singlets.

for the A_3 field – which must be done with care due to additional types of Feynman diagrams (ghosts, W loops, etc) – and verify that terms like $A_\mu^{(0)} Z^{(0)\mu} H^{(2k)}$ or $A_\mu^{(0)} A^{(0)\mu} H^{(2k)}$ do not exist as required by gauge invariance (A_μ represents the photon field).

Appendix D: Details on the photon flux from DM collisions in Schwarzschild BHs

The derivation and solutions of photon geodesics in the Schwarzschild metric can be found, e.g. in [127]. Here we discuss the case relevant for the gamma ray line signature we present in this work.

A non rotating BH is described by the Schwarzschild metric, which in spherical coordinates is

$$ds^2 = - \left(1 - \frac{r_S}{r} \right) dt^2 + \left(1 - \frac{r_S}{r} \right)^{-1} dr^2 + r^2 (d\theta^2 + \sin^2 \theta d\varphi^2), \quad (\text{D1})$$

where we have set $c = G = 1$ and $r_S = 2M_{\text{BH}}$ is the Schwarzschild radius. The four-velocity of a massive object is $u^\mu = dx^\mu / d\tau = (u^t, u^r, 0, u^\varphi)$ (when referring to the three-component velocity of a DM particle, v denotes the module of the velocity, while v_{rel} and v_{tan} denote the radial and tangential velocities). We indicate with k^μ the photon four-velocity.

As usual, the geodesics are defined as:

$$\frac{d^2 x^\alpha}{d\tau^2} + \Gamma_{\beta\gamma}^\alpha \frac{dx^\beta}{d\tau} \frac{dx^\gamma}{d\tau} = 0, \quad (\text{D2})$$

with $\Gamma_{\alpha\beta}^\gamma$ the Christoffel symbols and τ the proper time (replaced with the affine parameter λ for massless particles).

The three-velocity components and the module of the velocity of one DM particle, from Eq. (D1) and (D2), are

$$\begin{aligned} v_{\text{tot}} &= \frac{\sqrt{r^2 r_S + r_S l^2 - r l^2}}{r \sqrt{r}}, \\ v_{\text{rel}} &= \frac{l}{r} \sqrt{1 - \frac{r_S}{r}}, \\ v &= \sqrt{\frac{r_S}{r}}. \end{aligned} \quad (\text{D3})$$

The v_{tot} component, which is the velocity of the collided DM system, shows that the maximum allowed angular momentum for a particle falling into the BH is $|l| = 4$, otherwise dr/dt has a turning point before reaching the horizon. This demonstrates Eq. (26) and is shown in Fig. 6.

Let us consider now the photons, with both radial and angular motion, emitted by the DM system. Since both energy and angular momentum are conserved but γ 's are massless it is useful to introduce the impact parameter $b = L/E$. The photon geodesics are given by

$$\begin{aligned} \frac{dt}{d\lambda} &= \frac{1}{b} \left(1 - \frac{r_S}{r}\right)^{-1}, \\ \frac{dr}{d\lambda} &= \pm \frac{1}{b} \sqrt{1 - \frac{b^2}{B^2(r)}}, \\ \frac{d\varphi}{d\lambda} &= \frac{1}{r^2}, \end{aligned} \quad (\text{D4})$$

where $B^{-2}(r) = 1/r^2 (1 - r_S/r)$. The three-velocity components of the photons are

$$k_r = \sqrt{1 - \frac{b^2}{B^2(r)}} \quad \text{and} \quad k_t = \frac{b}{B}, \quad (\text{D5})$$

such that $k_r^2 + k_t^2 = 1$. Notice that only photons satisfying the following conditions can escape from the BH and reach far observers:

$$(1) \quad r < \frac{3}{2} r_S, k_r > 0, \sin \delta < \frac{3\sqrt{3}}{2} r_S (B(r))^{-1}, \quad (\text{D6})$$

$$(2) \quad r > \frac{3}{2} r_S, k_r > 0, \quad (\text{D7})$$

$$(3) \quad r < \frac{3}{2} r_S, k_r < 0, \sin \delta > \frac{3\sqrt{3}}{2} r_S (B(r))^{-1}, \quad (\text{D8})$$

where $\delta \equiv \arccos k_r \equiv \arcsin k_t$. Since the Schwarzschild BH can only provide a significant enhancement of CMS energy close to $r = r_S$, only Eq. (D6) is relevant. Notice that if the photon is emitted exactly at $r = r_S$, it has only a radial trajectory and the escape condition does not depend on its energy but only on the position r .

The initial conditions for the photon emitted from DM annihilation are given by Eq. (26) and by its velocity $\beta = v_{\text{rel}}$, equivalent to the relative velocity of the DM system. Let us first assume an observer which is comoving with the center of mass energy of the collision, hence stationary with respect to the collided system of two DM particles so that $u^t = 1/\sqrt{(1 - r_S/r)}$. The photon energy E_γ observed far away by the comoving observer is given by the gravitational redshift:

$$E_\gamma = E_\gamma^0 \sqrt{1 - \frac{r_S}{r}}. \quad (\text{D9})$$

We can then consider a stationary observer very far away from the BH, that sees the center of mass frame moving with velocity β , which gives the doppler shift effect added on top of the gravitational redshift. The frequency of the observed photon is

$$\omega = k^\alpha u_\alpha = g_{\alpha\beta} u^\alpha k^\beta = g_{tt} u^t k^t + g_{rr} u^r k^r, \quad (\text{D10})$$

where the $g_{\alpha\beta}$ are the components of the Schwarzschild metric. Equivalently, the observed photon energy is:

$$E_\gamma = E_\gamma^0 \sqrt{1 - \frac{r_S}{r}} \frac{\sqrt{1 - \beta^2}}{1 + \beta}. \quad (\text{D11})$$

More generally the Doppler shift can be a function of the angle δ (defined in Eqs. (D6 - D8)) between the emitted photon and the velocity of the source term

$$E_\gamma = E_\gamma^0 \sqrt{1 - \frac{r_S}{r}} \frac{\sqrt{1 - \beta^2}}{1 + v_{\text{tot}} \cos \delta}. \quad (\text{D12})$$

Note that the Doppler factor and the gravitational redshift factorize.

To account for all photons that can actually escape from the BH and reach the far observer along the line of sight on a small angle cone, we define a mean total redshift as

$$\begin{aligned} \bar{R}_{\text{tot}} &= \frac{1}{4\pi} \int (2\pi \, d\delta \sin \delta) \sqrt{1 - \frac{r_S}{r}} \frac{\sqrt{1 - \beta^2}}{1 + v_{\text{tot}} \cos \delta} \\ &\quad \times \Theta\left(\frac{3\sqrt{3}}{2} \frac{r_S}{r} \sqrt{1 - \frac{r_S}{r}} - \sin \delta\right), \end{aligned} \quad (\text{D13})$$

where the Θ function satisfies Eq. (D6). This can be rewritten as a function of $\cos \delta = x$,

$$\begin{aligned} \bar{R}_{\text{tot}} &= \frac{1}{2} \sqrt{1 - \frac{r_S}{r}} \sqrt{1 - \beta^2} \int_{x_{\text{min}}}^1 dx \frac{1}{1 + v_{\text{tot}} x} \\ &= \frac{1}{2v_{\text{tot}}} \sqrt{1 - \frac{r_S}{r}} \sqrt{1 - \beta^2} \log \left(\frac{1 + v_{\text{tot}}}{1 + v_{\text{tot}} x_{\text{min}}} \right), \end{aligned} \quad (\text{D14})$$

where x_{min} is determined by the Heavyside function. The mean redshift factor enters in the photon flux emitted by the BH, Eq. (31), and acts as a smearing factor.

-
- [1] G. Jungman, M. Kamionkowski, and K. Griest, *Phys.Rept.* **267**, 195 (1996), arXiv:hep-ph/9506380 [hep-ph].
- [2] L. Bergstrom, *Rept.Prog.Phys.* **63**, 793 (2000), arXiv:hep-ph/0002126 [hep-ph].
- [3] G. Bertone, D. Hooper, and J. Silk, *Phys.Rept.* **405**, 279 (2005), arXiv:hep-ph/0404175 [hep-ph].
- [4] T. Bringmann and C. Weniger, *Phys.Dark Univ.* **1**, 194 (2012), arXiv:1208.5481 [hep-ph].
- [5] T. Bringmann, F. Calore, G. Vertongen, and C. Weniger, *Phys.Rev.* **D84**, 103525 (2011), arXiv:1106.1874 [hep-ph].
- [6] L. Bergstrom, P. Ullio, and J. H. Buckley, *Astropart.Phys.* **9**, 137 (1998), arXiv:astro-ph/9712318 [astro-ph].
- [7] A. Birkedal, K. T. Matchev, M. Perelstein, and A. Spray, eprint (2005), arXiv:hep-ph/0507194 [hep-ph].
- [8] L. Bergstrom, T. Bringmann, M. Eriksson, and M. Gustafsson, *Phys.Rev.Lett.* **94**, 131301 (2005), arXiv:astro-ph/0410359 [astro-ph].
- [9] T. Bringmann, L. Bergstrom, and J. Edsjo, *JHEP* **0801**, 049 (2008), arXiv:0710.3169 [hep-ph].
- [10] A. Ibarra, S. Lopez Gehler, and M. Pato, *JCAP* **1207**, 043 (2012), arXiv:1205.0007 [hep-ph].
- [11] L. Bergstrom and P. Ullio, *Nucl.Phys.* **B504**, 27 (1997), arXiv:hep-ph/9706232 [hep-ph].
- [12] Z. Bern, P. Gondolo, and M. Perelstein, *Phys.Lett.* **B411**, 86 (1997), arXiv:hep-ph/9706538 [hep-ph].
- [13] P. Ullio and L. Bergstrom, *Phys.Rev.* **D57**, 1962 (1998), arXiv:hep-ph/9707333 [hep-ph].
- [14] L. Bergstrom, T. Bringmann, M. Eriksson, and M. Gustafsson, *JCAP* **0504**, 004 (2005), arXiv:hep-ph/0412001 [hep-ph].
- [15] T. Bringmann and F. Calore, (2013), arXiv:1308.1089 [hep-ph].
- [16] G. Nordstrom, *Phys. Z.* **15**, 504 (1914), arXiv:physics/0702221 [physics.gen-ph].
- [17] T. Kaluza, *Sitzungsber.Preuss.Akad.Wiss.Berlin (Math.Phys.)* **1921**, 966 (1921).
- [18] O. Klein, *Z.Phys.* **37**, 895 (1926).
- [19] D. Bailin and A. Love, *Rept.Prog.Phys.* **50**, 1087 (1987).
- [20] T. Appelquist, H.-C. Cheng, and B. A. Dobrescu, *Phys.Rev.* **D64**, 035002 (2001), arXiv:hep-ph/0012100 [hep-ph].
- [21] H.-C. Cheng, K. T. Matchev, and M. Schmaltz, *Phys.Rev.* **D66**, 036005 (2002), arXiv:hep-ph/0204342 [hep-ph].
- [22] A. Belyaev, M. Brown, J. Moreno, and C. Papineau, *JHEP* **1306**, 080 (2013), arXiv:1212.4858.
- [23] G. Servant and T. M. Tait, *Nucl.Phys.* **B650**, 391 (2003), arXiv:hep-ph/0206071 [hep-ph].
- [24] H.-C. Cheng, J. L. Feng, and K. T. Matchev, *Phys.Rev.Lett.* **89**, 211301 (2002), arXiv:hep-ph/0207125 [hep-ph].
- [25] A. Datta, K. Kong, and K. T. Matchev, *Phys.Rev.* **D72**, 096006 (2005), arXiv:hep-ph/0509246 [hep-ph].
- [26] C.-R. Chen, M. M. Nojiri, S. C. Park, J. Shu, and M. Takeuchi, *JHEP* **0909**, 078 (2009), arXiv:0903.1971 [hep-ph].
- [27] G. Cacciapaglia, A. Deandrea, J. Ellis, J. Marrouche, and L. Panizzi, *Phys.Rev.* **D87**, 075006 (2013), arXiv:1302.4750 [hep-ph].
- [28] G. Servant, (2014), arXiv:1401.4176 [hep-ph].
- [29] G. Servant and T. M. Tait, *New J.Phys.* **4**, 99 (2002), arXiv:hep-ph/0209262 [hep-ph].
- [30] G. Bertone, D. G. Cerdeno, J. Collar, and B. C. Odom, *Phys.Rev.Lett.* **99**, 151301 (2007), arXiv:0705.2502 [astro-ph].
- [31] S. Arrenberg, L. Baudis, K. Kong, K. T. Matchev, and J. Yoo, *Phys.Rev.* **D78**, 056002 (2008), arXiv:0805.4210 [hep-ph].
- [32] S. Arrenberg, L. Baudis, K. Kong, K. T. Matchev, and J. Yoo, (2013), arXiv:1307.6581.
- [33] G. Bertone, G. Servant, and G. Sigl, *Phys.Rev.* **D68**, 044008 (2003), arXiv:hep-ph/0211342 [hep-ph].
- [34] G. Bertone, C. Jackson, G. Shaughnessy, T. M. Tait, and A. Vallinotto, *JCAP* **1203**, 020 (2012), arXiv:1009.5107 [astro-ph.HE].
- [35] D. Hooper and G. D. Kribs, *Phys.Rev.* **D70**, 115004 (2004), arXiv:hep-ph/0406026 [hep-ph].
- [36] E. A. Baltz and D. Hooper, *JCAP* **0507**, 001 (2005), arXiv:hep-ph/0411053 [hep-ph].
- [37] D. Hooper and K. M. Zurek, *Phys.Rev.* **D79**, 103529 (2009), arXiv:0902.0593 [hep-ph].
- [38] D. Hooper and G. D. Kribs, *Phys.Rev.* **D67**, 055003 (2003), arXiv:hep-ph/0208261 [hep-ph].
- [39] T. Flacke, A. Menon, D. Hooper, and K. Freese, (2009), arXiv:0908.0899 [hep-ph].
- [40] M. Blennow, H. Melbeus, and T. Ohlsson, *JCAP* **1001**, 018 (2010), arXiv:0910.1588 [hep-ph].
- [41] G. Bertone, K. Kong, R. R. de Austri, and R. Trotta, *Phys.Rev.* **D83**, 036008 (2011), arXiv:1010.2023 [hep-ph].
- [42] T. Bringmann, *JCAP* **0508**, 006 (2005), arXiv:astro-ph/0506219 [astro-ph].
- [43] A. Barrau, P. Salati, G. Servant, F. Donato, J. Grain, *et al.*, *Phys.Rev.* **D72**, 063507 (2005), arXiv:astro-ph/0506389 [astro-ph].
- [44] D. Hooper and S. Profumo, *Phys.Rept.* **453**, 29 (2007), arXiv:hep-ph/0701197 [hep-ph].
- [45] M. Kakizaki, S. Matsumoto, Y. Sato, and M. Senami, *Phys.Rev.* **D71**, 123522 (2005), arXiv:hep-ph/0502059 [hep-ph].
- [46] M. Battaglia, A. Datta, A. De Roeck, K. Kong, and K. T. Matchev, *JHEP* **0507**, 033 (2005), arXiv:hep-ph/0502041 [hep-ph].
- [47] B. Bhattacharjee and A. Kundu, *Phys.Lett.* **B627**, 137 (2005), arXiv:hep-ph/0508170 [hep-ph].
- [48] S. Matsumoto, J. Sato, M. Senami, and M. Yamanaka, *Phys.Rev.* **D80**, 056006 (2009), arXiv:0903.3255 [hep-ph].
- [49] M. Kakizaki, S. Matsumoto, Y. Sato, and M. Senami, *Nucl.Phys.* **B735**, 84 (2006), arXiv:hep-ph/0508283 [hep-ph].
- [50] M. Kakizaki, S. Matsumoto, and M. Senami, *Phys.Rev.* **D74**, 023504 (2006), arXiv:hep-ph/0605280 [hep-ph].
- [51] J. M. Cornell, S. Profumo, and W. Shepherd, (2014), arXiv:1401.7050 [hep-ph].
- [52] A. Baushev, eprint (2008), arXiv:0805.0124 [astro-ph].
- [53] M. Banados, J. Silk, and S. M. West, *Phys.Rev.Lett.* **103**, 111102 (2009), arXiv:0909.0169 [hep-ph].

- [54] M. Banados, B. Hassanain, J. Silk, and S. M. West, *Phys.Rev.* **D83**, 023004 (2011), arXiv:1010.2724 [astro-ph.CO].
- [55] A. J. Williams, *Phys.Rev.* **D83**, 123004 (2011), arXiv:1101.4819 [astro-ph.CO].
- [56] M. Cannoni, M. Gomez, M. Perez-Garcia, and J. Vergados, *Phys.Rev.* **D85**, 115015 (2012), arXiv:1205.1709 [hep-ph].
- [57] A. Grib, Y. Pavlov, and O. Piattella, *Grav.Cosmol.* **18**, 70 (2012), arXiv:1203.4952 [gr-qc].
- [58] M. Patil and P. S. Joshi, *Phys.Rev.* **D86**, 044040 (2012), arXiv:1203.1803 [gr-qc].
- [59] T. Harada, H. Nemoto, and U. Miyamoto, *Phys.Rev.* **D86**, 024027 (2012), arXiv:1205.7088 [gr-qc].
- [60] T. Jacobson and T. P. Sotiriou, *Phys.Rev.Lett.* **104**, 021101 (2010), arXiv:0911.3363 [gr-qc].
- [61] E. Berti, V. Cardoso, L. Gualtieri, F. Pretorius, and U. Sperhake, *Phys.Rev.Lett.* **103**, 239001 (2009), arXiv:0911.2243 [gr-qc].
- [62] S. T. McWilliams, *Phys.Rev.Lett.* **110**, 011102 (2013), arXiv:1212.1235 [gr-qc].
- [63] F. Aharonian *et al.* (H.E.S.S. Collaboration), *Astron.Astrophys.* **457**, 899 (2006), arXiv:astro-ph/0607333 [astro-ph].
- [64] B. Acharya, M. Actis, T. Aghajani, G. Agnetta, J. Aguilar, *et al.*, *Astropart.Phys.* **43**, 3 (2013).
- [65] H.-C. Cheng, K. T. Matchev, and M. Schmaltz, *Phys.Rev.* **D66**, 056006 (2002), arXiv:hep-ph/0205314 [hep-ph].
- [66] L. Edelhauser, T. Flacke, and M. Kramer, *JHEP* **1308**, 091 (2013), arXiv:1302.6076 [hep-ph].
- [67] T. Kakuda, K. Nishiwaki, K.-y. Oda, N. Okuda, and R. Watanabe, (2013), arXiv:1304.6362 [hep-ph].
- [68] T. Kakuda, K. Nishiwaki, K.-y. Oda, and R. Watanabe, *Phys.Rev.* **D88**, 035007 (2013), arXiv:1305.1686 [hep-ph].
- [69] G. von Gersdorff, N. Irges, and M. Quiros, *Nucl.Phys.* **B635**, 127 (2002), arXiv:hep-th/0204223 [hep-th].
- [70] H. Georgi, A. K. Grant, and G. Hailu, *Phys.Lett.* **B506**, 207 (2001), arXiv:hep-ph/0012379 [hep-ph].
- [71] G. Aad *et al.* (ATLAS Collaboration), *Phys.Lett.* **B716**, 1 (2012), arXiv:1207.7214 [hep-ex].
- [72] S. Chatrchyan *et al.* (CMS Collaboration), *Phys.Lett.* **B716**, 30 (2012), arXiv:1207.7235 [hep-ex].
- [73] M. Blennow, H. Melbeus, T. Ohlsson, and H. Zhang, *Phys.Lett.* **B712**, 419 (2012), arXiv:1112.5339 [hep-ph].
- [74] G. Belanger, M. Kakizaki, and A. Pukhov, *JCAP* **1102**, 009 (2011), arXiv:1012.2577 [hep-ph].
- [75] T. Flacke, K. Kong, and S. C. Park, *JHEP* **1305**, 111 (2013), arXiv:1303.0872 [hep-ph].
- [76] T. Flacke, A. Menon, and D. J. Phalen, *Phys.Rev.* **D79**, 056009 (2009), arXiv:0811.1598 [hep-ph].
- [77] K. Kong and K. T. Matchev, *JHEP* **0601**, 038 (2006), arXiv:hep-ph/0509119 [hep-ph].
- [78] F. Burnell and G. D. Kribs, *Phys.Rev.* **D73**, 015001 (2006), arXiv:hep-ph/0509118 [hep-ph].
- [79] J. F. Beacom, N. F. Bell, and G. Bertone, *Phys.Rev.Lett.* **94**, 171301 (2005), arXiv:astro-ph/0409403 [astro-ph].
- [80] A. Galper, O. Adriani, R. Aptekar, I. Arkhangelskaja, A. Arkhangelskiy, *et al.*, *AIP Conf.Proc.* **1516**, 288 (2012), arXiv:1210.1457 [astro-ph.IM].
- [81] DAMPE, <http://dpnc.unige.ch/dampe/index.html>.
- [82] N. Mori (CALET Collaboration), *Nucl. Phys. Proc. Suppl.* **239-240**, 199 (2013).
- [83] J. Bonnevier, H. Melbeus, A. Merle, and T. Ohlsson, *Phys.Rev.* **D85**, 043524 (2012), arXiv:1104.1430 [hep-ph].
- [84] L. Landau, *Dokl.Akad.Nauk Ser.Fiz.* **60**, 207 (1948).
- [85] C.-N. Yang, *Phys.Rev.* **77**, 242 (1950).
- [86] P. Salucci, F. Nesti, G. Gentile, and C. Martins, *Astron.Astrophys.* **523**, A83 (2010), arXiv:1003.3101 [astro-ph.GA].
- [87] J. Bovy and S. Tremaine, *Astrophys.J.* **756**, 89 (2012), arXiv:1205.4033 [astro-ph.GA].
- [88] J. F. Navarro, C. S. Frenk, and S. D. White, *Astrophys.J.* **462**, 563 (1996), arXiv:astro-ph/9508025 [astro-ph].
- [89] J. Diemand, M. Kuhlen, P. Madau, M. Zemp, B. Moore, *et al.*, *Nature* **454**, 735 (2008), arXiv:0805.1244 [astro-ph].
- [90] J. Diemand, M. Zemp, B. Moore, J. Stadel, and M. Carollo, *Mon.Not.Roy.Astron.Soc.* **364**, 665 (2005), arXiv:astro-ph/0504215 [astro-ph].
- [91] J. Stadel, D. Potter, B. Moore, J. Diemand, P. Madau, *et al.*, *Mon. Not. Roy. Astron. Soc.* **398**, L21 (2009), arXiv:0808.2981 [astro-ph].
- [92] R. K. de Naray and K. Spekkens, *Astrophys.J.* **741**, L29 (2011), arXiv:1109.1288 [astro-ph.CO].
- [93] M. G. Walker and J. Penarrubia, *Astrophys.J.* **742**, 20 (2011), arXiv:1108.2404 [astro-ph.CO].
- [94] P. Gondolo and J. Silk, *Phys.Rev.Lett.* **83**, 1719 (1999), arXiv:astro-ph/9906391 [astro-ph].
- [95] G. Bertone and D. Merritt, *Mod.Phys.Lett.* **A20**, 1021 (2005), arXiv:astro-ph/0504422 [astro-ph].
- [96] G. Bertone and D. Merritt, *Phys.Rev.* **D72**, 103502 (2005), arXiv:astro-ph/0501555 [astro-ph].
- [97] L. Sadeghian, F. Ferrer, and C. M. Will, *Phys.Rev.* **D88**, 063522 (2013), arXiv:1305.2619 [astro-ph.GA].
- [98] O. Y. Gnedin and J. R. Primack, *Phys.Rev.Lett.* **93**, 061302 (2004), arXiv:astro-ph/0308385 [astro-ph].
- [99] E. Vasiliev and M. Zelnikov, *Phys.Rev.* **D78**, 083506 (2008), arXiv:0803.0002 [astro-ph].
- [100] J. Binney and S. Tremaine, *Galactic Dynamics* (Princeton University Press, 1987).
- [101] F. Ferrer and D. R. Hunter, *JCAP* **1309**, 005 (2013), arXiv:1306.6586 [astro-ph.HE].
- [102] F.-S. Ling, E. Nezri, E. Athanassoula, and R. Teyssier, *JCAP* **1002**, 012 (2010), arXiv:0909.2028 [astro-ph.GA].
- [103] T. Do, G. D. Martinez, S. Yelda, A. Ghez, J. Bullock, M. Kaplinghat, J. R. Lu, A. H. G. Peter, and K. Phifer, *Astrophys.J.Lett.* **779**, L6 (2013), arXiv:1311.0886 [astro-ph.GA].
- [104] R. Schodel, A. Feldmeier, D. Kunneriath, S. Stolovy, N. Neumayer, *et al.*, (2014), arXiv:1403.6657 [astro-ph.GA].
- [105] A. Abramowski *et al.* (H.E.S.S. Collaboration), *Phys.Rev.Lett.* **110**, 041301 (2013), arXiv:1301.1173 [astro-ph.HE].
- [106] G. Pedalletti, "Presentation at the Workshop on the Future of Dark Matter Astro-Particle Physics in Trieste," <http://cdsagenda5.ictp.trieste.it/askArchive.php?base=agenda&categ=a12213&id=a12213s82t70/slides> (2013).
- [107] A. Pinzke, C. Pfrommer, and L. Bergstrom, *Phys.Rev.* **D84**, 123509 (2011), arXiv:1105.3240 [astro-ph.HE].
- [108] M. A. Sanchez-Conde, M. Cannoni, F. Zandanel, M. E.

- Gomez, and F. Prada, *JCAP* **1112**, 011 (2011), arXiv:1104.3530 [astro-ph.HE].
- [109] S. Maurogordato, A. Cappi, C. Ferrari, C. Benoist, G. Mars, G. Soucail, M. Arnaud, G. W. Pratt, H. Bourdin, and J.-L. Sauvageot, *Astronomy and Astrophysics* **481**, 593 (2008), arXiv:0712.2715.
- [110] M. Bejger, T. Piran, M. Abramowicz, and F. Håkanson, *Physical Review Letters* **109**, 121101 (2012), arXiv:1205.4350 [astro-ph.HE].
- [111] O. B. Zaslavskii, *Journal of High Energy Physics* **12**, 32 (2012), arXiv:1209.4987 [gr-qc].
- [112] A. Grib and Y. Pavlov, *Grav.Cosmol.* **17**, 42 (2011), arXiv:1010.2052 [gr-qc].
- [113] I. Tanatarov and O. Zaslavskii, *Phys.Rev.* **D88**, 064036 (2013), arXiv:1307.0034 [gr-qc].
- [114] O. Zaslavskii, *Phys.Rev.Lett.* **111**, 079001 (2013), arXiv:1301.3429.
- [115] J. Gariel, G. Marilhacy, and N. O. Santos, *ApJ* **774**, 109 (2013), arXiv:1303.6474 [astro-ph.HE].
- [116] T. Harada, H. Nemoto, and U. Miyamoto, *Phys.Rev.* **D86**, 024027 (2012), arXiv:1205.7088 [gr-qc].
- [117] O. Zaslavskii, *Phys.Rev.* **D86**, 084030 (2012), arXiv:1205.4410 [gr-qc].
- [118] O. Zaslavskii, (2013), arXiv:1305.6136 [gr-qc].
- [119] J. Kormendy and L. C. Ho, *ArXiv e-prints* (2013), arXiv:1304.7762 [astro-ph.CO].
- [120] J. Kormendy and R. Bender, *ApJS* **198**, 2 (2012), arXiv:1110.4384 [astro-ph.CO].
- [121] J. M. Bardeen, W. H. Press, and S. A. Teukolsky, *Astrophys.J.* **178**, 347 (1972).
- [122] R. Mertig, M. Bohm, and A. Denner, *Comput.Phys.Commun.* **64**, 345 (1991).
- [123] T. Hahn and M. Perez-Victoria, *Comput. Phys. Commun.* **118**, 153 (1999), arXiv:hep-ph/9807565 [hep-ph].
- [124] T. Bringmann, PhD thesis, Stockholm University (2005), ISBN 91-7155-117-4.
- [125] M. Gustafsson, PhD thesis, Stockholm University (2008), ISBN 978-91-7155-548-9.
- [126] G. Passarino and M. Veltman, *Nucl.Phys.* **B160**, 151 (1979).
- [127] C. W. Misner, K. Thorne, and J. Wheeler, (1974).